Studies on the separation of Z and Higgs boson using polarisation observables

Cedric Carl Breuning

Bachelorarbeit in Physik
angefertigt im Physikalischen Institut

vorgelegt der
Mathematisch-Naturwissenschaftlichen Fakultät
der
Rheinischen Friedrich-Wilhelms-Universität
Bonn

Oktober 2022

Ich versichere, dass ich diese Arbeit selbstständig verfasst und keine anderen als die angegebenen Quellen und Hilfsmittel benutzt sowie die Zitate kenntlich gemacht habe.

Bonn, ...

Datum Unterschrift

1. Gutachter: Prof. Dr. Klaus Desch
2. Gutachterin: Priv.-Doz. Dr. Philip Bechtle

Acknowledgements

I would like to thank Prof. Dr. Klaus Desch for providing me with the opportunity to conduct research and write my thesis on this very interesting topic. I would also like to thank Priv.-Doz. Dr. Philip Bechtle and Dr. Christian Grefe for helping me throughout this thesis. Another thank you to all other members of Prof. Desch's ATLAS data analysis group for the pleasant working atmosphere.

A special thank you to Anne-Kathrin Mahlke and Valerie Mauth for reading this thesis and providing valuable feedback. Lastly I want to thank my family and friends for keeping me motivated and supporting me.

Contents

CHAPTER 1

Introduction

To explain the world around us scientist have developed, improved and expanded many theories. Conducting experiments, they try to verify or disprove these theories. One theory that aims to explain our world using elementary particles is the Standard Model of particle physics (SM). SM predictions have been successfully validated in many experiments, for example the existence of the top quark [1] or the discovery of the Higgs boson in 2012 [2, 3]. But even though the SM is able to describe a wide range of experimental results, there are still unanswered questions. Examples are the unification of the fundamental forces or an explanation for dark matter [4]. To explain these and other Beyond the Standard Model (BSM) phenomena, the SM is expanded, adapted or other theories are created. Other models have adapted the number of Higgs bosons compared to the SM, which has only one Higgs boson. The Minimal Supersymmetric extension of the Standard Model (MSSM), for example, predicts multiple Higgs bosons [5].

The Compact Muon Solenoid (CMS) experiment at the European Organization for Nuclear Research (CERN) observed an excess in the $\tau\tau$ channel that could potentially correspond to another Higgs boson. This excess is shown in Fig. 1.1 and has a global p-value of $2.7\,\sigma$ at a mass of $m_\phi = 100\,\text{GeV}$. CMS also found an excess in the $\gamma\gamma$ channel with a significance of $2.8\,\sigma$ at a mass of 95.3 GeV, that coincides with the $\tau\tau$ excess within the $m_{\tau\tau}$ resolution [6, 7].

A major problem in analysing this excess is the background from $Z \to \tau\tau$ processes because $m_Z = 91.2\,\text{GeV}$ is close to the mass where the excess was measured. The mass is an observable that is used in many analyses to find or identify particles (for example in [6, 8]). When searching for Higgs bosons with a Z background, the particle mass is not the only property that is different for these two particles. They also differ in their spin (Z has spin 1, the Higgs boson has spin 0), and because angular momentum is conserved, it should be possible to access this information via the polarisation of the Z and Higgs boson decay products.

The goal of this thesis is to find and analyse a polarisation observable that is directly calculated from the H and Z decay products. The analysis focuses on the $\tau\tau$ channel. The analysed polarisation observable should indicate whether the initial state particle could have been a Higgs boson. This would be especially useful for analyses close to the Z mass but could also prove useful for a SM Higgs analysis.

This thesis is structured as follows: The theoretical background and the basic idea of the polarisation observable, that will be used, are presented in Chapter 2 followed by the experimental setup at CERN in Chapter 3. Because this thesis uses simulated data from the A Toroidal LHC ApparatuS (ATLAS)

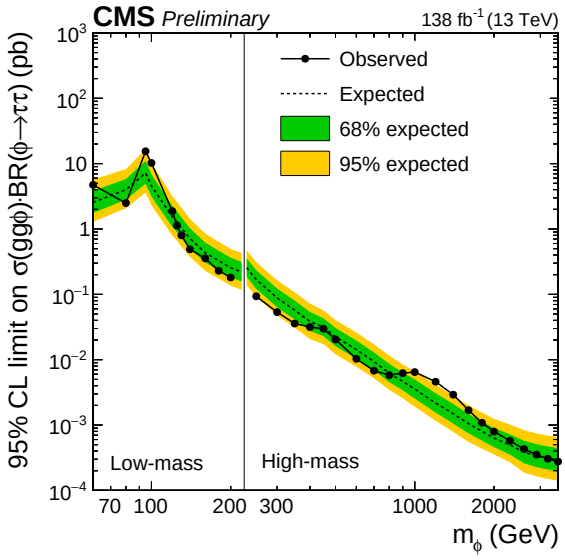

Figure 1.1: Observed and expected 95 % confidence level (CL) upper limit for the product of cross section (σ) and branching fraction (BR) for $gg\phi \rightarrow \tau\tau$ in a mass range of $60 \leq m_{\phi} \leq 3\,500$ GeV. The variable ϕ is a resonance in addition to the observed Higgs boson [6].

experiment, Chapter 4 explains how the used data is generated and which selection cuts are applied to the data. In Chapter 5 the analysis of the polarisation observable is described. Chapter 6 will summarise the results and Chapter 7 will give an overview on how the results may be improved and some possible next steps.

CHAPTER 2

Theory

2.1 The Standard Model of particle physics

The SM is a theoretical model that describes the interaction between fundamental particles. This section provides a short overview of the SM based on [4] and explains the underlying concepts and effects. The elementary particles used in the SM and some of their properties are illustrated in Fig. 2.1.

Matter is formed by fermions, the elementary SM particles with spin $1/2$. A fermion is either a quark that carries, among other things, colour charge and fractional electric charge Q, or a lepton that does not carry colour charge and has integer electric charge. Quarks q and leptons ℓ are split into three generations. The fermions of the next generation are copies of the fermions in the current generation with higher mass. Each generation consists of one up-type quark ($Q = +2/3$), one down-type quark ($Q = -1/3$), one electron-like lepton ($Q = -1$) and the corresponding neutrino ν ($Q = 0$). These four particles in three generations add up to the twelve fermions in the SM. The fermions in the first generation are stable. Each fermion has an antiparticle with opposite electric charge and for quarks also anticolours as colour charge. A particle and the corresponding antiparticle can be produced together, and when they collide they can annihilate.

The fundamental interactions are carried out by the gauge bosons. In the SM, these bosons are the gluon g, the photon γ, the Z and $W^{\pm}$, which all have spin 1. The last particle, H (Higgs boson), is a consequence of the Higgs mechanism that is needed to give mass to the Z and $W^{\pm}$. The fundamental interactions and the Higgs mechanism are described below.

Strong interaction

Particles with colour charge, quarks and gluons, can interact via the strong interaction that is described by Quantum Chromodynamics (QCD) with g as mediating boson. One QCD effect that is relevant here is confinement: particles that carry colour charge cannot occur isolated. If a particle decays into quarks, the decay product needs to be some bound QCD state that is colour neutral. Therefore, quarks form hadrons that can be observed in an experiment. Another relevant effect is the emission of gluons from quarks or other gluons. These radiated g can produce a cone of hadrons, a so called jet.

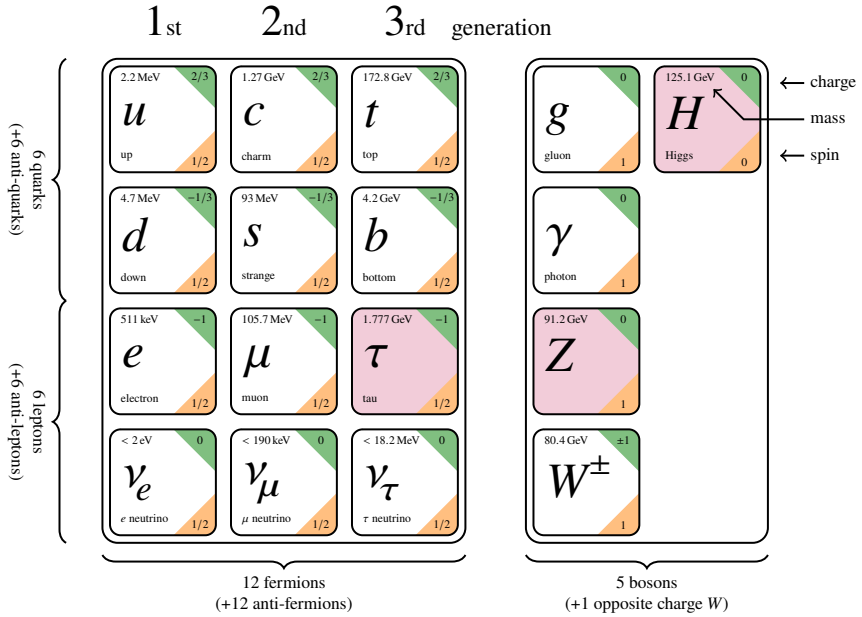

Figure 2.1: Overview of elementary SM particles. The red highlighted particles are of special interest for this thesis. Figure adapted from [9], data taken from [10].

Electromagnetic interaction

Interactions between particles with electric charge can be described by Quantum Electrodynamics (QED) with γ as mediating boson. This interaction can be unified with the weak interaction. QED is not relevant for this thesis as an independent interaction.

Weak interaction

All fermions can interact via the weak interaction. There are weak charged currents (interaction including $W^{\pm}$) or weak neutral currents (interaction including Z). One example for such an interaction is the τ decay via weak charged currents.

Gravity

Gravity is particularly important for large structures (for example stars and planets) but is not explained by the SM. A potential mediating boson (graviton) hasn't been found so far. On the scale of particles gravity becomes so weak that it is neglected.

Higgs mechanism

The weak and electromagnetic interaction can be unified into the electroweak interaction as a gauge group. The mediating bosons are $W^{\pm}$, Z and γ. The masses of the gauge bosons need to be zero because a mass term in the Lagrangian would violate the required gauge invariance [5], but Z and $W^{\pm}$ have high masses. To solve this problem Higgs [11], Englert and Brout [12] proposed a model known

today as Higgs mechanism. The Higgs field (complex Higgs doublet) is introduced and all gauge bosons are massless. After symmetry breaking, the vacuum expectation value of the Higgs field is non-zero. This leads to mass terms in the Lagrangian that correspond to the $W^{\pm}$ and Z masses. Other terms correspond to the mass and interaction of a scalar boson, the Higgs boson H [5]. The fermion masses are generated with Yukawa coupling through the same scalar field. Yukawa coupling also introduces coupling between H and fermions. The spin 0 particle H couples to fermion antifermion pairs (the $H \rightarrow \tau^{+}\tau^{-}$ decay is of particular importance for this thesis), $W^{+}W^{-}$ and Z pairs. The coupling strength of a particle x to H is proportional to the mass m_x of the particle [13]. A H can also decay into a pair of photons, even though the photon is massless and the H has no electric charge. This is possible through other particles. The H decays into a charged particle and its antiparticle. They can then produce two photons. The H does not couple to gluons but can be produced in hadron-hadron collisions by two gluons. The gluons can produce quarks, a quark antiquark pair, that can then annihilate and produce a H. This process is called gluon fusion (ggF) and the corresponding leading-order (LO) Feynman diagram is shown in Fig. 2.2. The quarks in this scenario are typically top quarks because of their high mass [13].

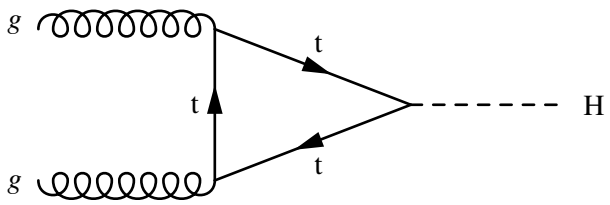

Figure 2.2: Leading-order Feynman diagram of ggF H production. Two gluons g produce a H through a top quark t loop.

2.2 Beyond the Standard Model Higgs bosons

For the SM described above, one single Higgs boson is sufficient but SM versions (extensions) with more Higgs doublets and more Higgs bosons are also possible. The MSSM is such a model and possesses two Higgs doublets [5]. However, the excess in the $\gamma\gamma$ channel that was found in [7] is not explained by this model. The measured cross section does not fit into the range predicted by Bechtle et al. [14]. As a potential explanation [15] found that the $\gamma\gamma$ excess can be explained by the Next-to-MSSM (NMSSM) that extends the MSSM by an extra scalar singlet field [16].

For the $\tau\tau$ channel the expected MSSM cross section can be estimated for the expected mass of the BSM H around 95 GeV. The coupling in Fig. 2.3 is SM normalized and for this mass approximately 1. Thus, a BSM H that couples to two gluons, via a top or bottom quark loop, like the SM H can be considered. The cross section for producing such a BSM H at this mass for $\sqrt{s} = 13$ TeV is $\sigma = 68.25$ pb [17]. With a branching fraction of approximately 0.22 (Fig. 2.3) the estimated cross section is 15.015 pb. The $\tau\tau$ channel excess at a mass of 100 GeV has an upper limit for the cross section of approximately 11 pb [6]. This is lower than the estimated cross section. However, the

calculation based on Fig. 2.3 was just an approximation and used a slightly lower mass than the mass of the found excess. Thus, it may be possible that this excess is explained by the MSSM. However, this is not necessarily the correct explanation for this excess. There could be other theories that also explain this excess or this excess has some other origin.

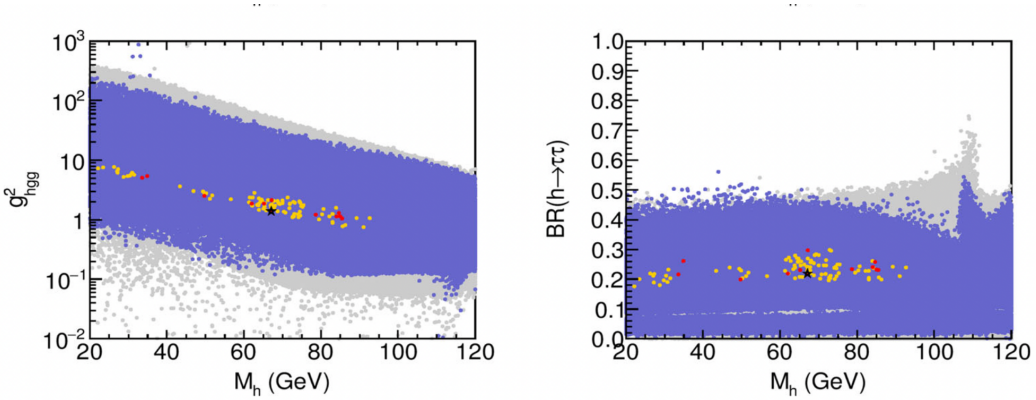

Figure 2.3: SM normalized hgg coupling (left) and $h \to \tau\tau$ branching fraction (BR, right) for a light Higgs boson h in dependence of its mass. The gray points are all scanned points, the blue ones fit specific Higgs search and LHC sparticle search constraints and the yellow ones show favoured regions [14].

2.3 The tau lepton

The tau lepton (τ-lepton) was discovered 1975 by Perl et al. [18]. It is the heaviest lepton in the SM with a mass of $m_\tau = (1\,776.86 \pm 0.12)$ MeV [10]. This high mass results in the strongest coupling to H within the leptons so the most likely leptonic H decay is $H \to \tau^+\tau^-$.

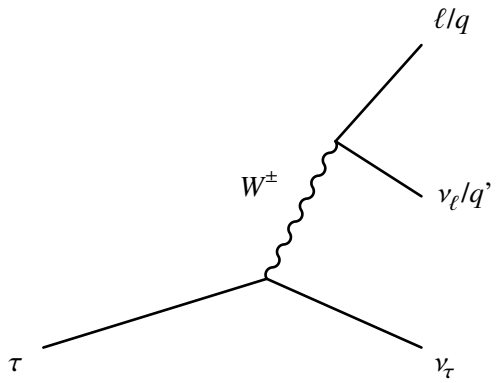

Figure 2.4: Leading-order Feynman diagram for τ decays. The τ can decay leptonically ($\tau^- \to \ell^-\overline{\nu}_\ell\nu_\tau$ or $\tau^+ \to \ell^+\nu_\ell\overline{\nu}_\tau$ where $\ell \in \{e, \mu\}$) or hadronically ($\tau^- \to q\overline{q}'\nu_\tau$ or $\tau^+ \to \overline{q}q'\overline{\nu}_\tau$ where q is a down-type and q' an up-type quark).

The τ decays via the weak interaction producing a ν_τ and a $W^\pm$ that can decay into a lepton ℓ ($\ell \in \{e, \mu\}$) and the corresponding neutrino ν_ℓ or quarks that form a light enough hadron. The hadronic decay is possible due to the high τ mass. Fig. 2.4 shows the LO Feynman diagram for the τ decay.

The hadronic τ decay can form multiple charged hadrons (mostly $\pi^{\pm}$ and sometimes $K^{\pm}$) in the final state [10]. A decay with N charged hadrons in the final state is referred to as N-prong (Np). Besides the charged hadrons, multiple neutral pions π^0 can be produced. Thus, a hadronic τ decay mode can be classified using the number of charged hadrons N and the number of neutral pions M in the final state and is named $N\mathrm{p}M\mathrm{n}$ [19]. The branching fractions for dominant hadronic and the leptonic decay modes are shown in Table 2.1.

Table 2.1: Branching fractions Γ_i/Γ for the dominant τ decay modes d taken from [10]. The leptonic decay modes show τ^- decays but the branching fractions are the same for τ^+ decays. In each decay a ν_τ is produced but it is not written with the decay modes here.

	Decay mode d	Γ_i/Γ
Leptonic	$e^-\overline{\nu}_e$	$(17.82 \pm 0.04)\,\%$
	$\mu^-\overline{\nu}_\mu$	$(17.39 \pm 0.04)\,\%$
Hadronic	1p0n	$(11.51 \pm 0.05)\,\%$
	1p1n	$(25.93 \pm 0.09)\,\%$
	1p(≥2)n	$(10.81 \pm 0.09)\,\%$
	3p0n	$(9.80 \pm 0.05)\,\%$
	3p(≥1)n	$(5.29 \pm 0.05)\,\%$

2.3.1 Tau polarisation

Because of the short τ lifetime the average travelling distance of a τ is only about 87.03 µm [10]. However, in the ATLAS experiment they are highly boosted, which increases this distance significantly. But for H and Z decays the vast majority of τ-leptons decay in the beam pipe before they reach the first detector. Thus, only the τ decay products, in hadronic decays in the form of jets, are measured and the τ properties have to be reconstructed [20]. The decay products provide access to the τ helicity. Assuming the relativistic limit where m_τ can be neglected, the helicity state of a τ matches its chiral state. Also assuming collinear τ decay products, the helicity states can be called left-handed and right-handed [21]. If momentum and spin point in the same direction, the helicity state is called right-handed, if they point in opposite directions the helicity state is called left-handed. Due to parity violation in the weak interaction, neutrinos are always left-handed and antineutrinos are always right-handed [13].

This thesis focuses on the 1p1n decay with the highest branching ratio among the hadronic decays. Thus, there are many events that can be used in the analysis and there is an observable that highly depends on the τ helicity. In almost all 1p1n decays the τ decays via the ρ resonance into a charged and a neutral pion. The ρ has spin 1 [10]. Let the the quantisation axis a be the boost direction and write the spin J states of the particles as (J, J_a). The ρ can be polarised transversally (here: spin orientation parallel or antiparallel to its flight direction, spin state $(1, \pm 1)$) or longitudinally (here: spin orientation perpendicular to its flight direction, spin state $(1, 0)$). To conserve angular momentum, the ν_τ spin $(1/2, \pm 1/2)$ and the ρ spin have to add up to the τ spin $(1/2, \pm 1/2)$. Because of the handedness constraint on neutrinos, there are two possible cases for the $\tau^- \to \rho^-\nu_\tau$ decay for a left-handed τ^- that are shown in Fig. 2.5. For a right-handed τ^- the τ^- in this figure is boosted in the opposite direction but the flight directions of the decay products and all spin orientations stay the same as

before. Therefore, the longitudinal ρ^- is emitted in the τ^- flight direction and the transverse ρ^-, in the opposite direction. The decays where the ρ^- is emitted in the τ^- direction of flight are favoured. Thus, a left-handed τ^- will preferably decay into a transverse ρ^- and a right-handed τ^- into a longitudinal ρ^- [22, 23].

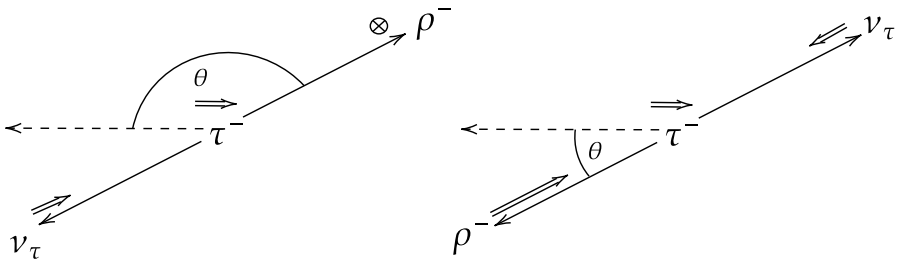

Figure 2.5: Two possible helicity configurations in the $\tau^- \rightarrow \rho^- \nu_\tau$ decay for a left-handed τ^-. Solid arrows with a single line indicate flight direction, solid arrows with a double line spin orientation and $\otimes$ indicates longitudinal polarisation. The dashed arrows show the boost direction of the τ^-. The decay angle is θ.

The ρ^- is not the detected particle but decays further into a π^0 and a π^- (sometimes a K^-). The pions are emitted back-to-back and have spin 0 so the ρ^- spin is transformed to angular momentum. Because of that the pions are emitted perpendicular to the ρ^- spin. As shown in Fig. 2.6, the pions from a transverse polarised ρ^- are emitted perpendicular to the ρ^- flight direction. These pions will have approximately the same energy. For longitudinal polarisation one pion (charged or neutral) is emitted more parallel to the ρ^- flight direction and the other one in the opposite direction. In a boosted system, one pion in this decay will have high and the other one low energy [21, 23]. The charged energy asymmetry [21]

$$\Upsilon_- = \frac{E_{\pi^-} - E_{\pi^0}}{E_{\pi^-} + E_{\pi^0}} \tag{2.1}$$

can be used to gain information on the ρ^- and thus the τ^- helicity by taking advantage of the energy symmetry in the transverse and asymmetry in the longitudinal decay. This means Υ_- will preferably be 0 for a transverse ρ^- and thus a probably left-handed τ^-. A right-handed τ^- will most likely decay into a longitudinal ρ^- and therefore Υ_- is most likely going to be around +1 or −1.

Eq. (2.1) can be extended to

$$\Upsilon_\pm = \frac{E_{\pi^\pm} - E_{\pi^0}}{E_{\pi^\pm} + E_{\pi^0}} \tag{2.2}$$

and will also work for τ^+ decays. A τ^+ will decay analogously to a τ^- with the corresponding antiparticles as decay products. Because in this decay an antineutrino, that needs to be right-handed, is produced the energy symmetry and asymmetry is exactly opposite to the τ^- decay. Therefore, Υ_+ will preferably be 0 for a right-handed τ^+ and +1 or −1 for a left-handed τ^+.

Figure 2.7 shows what $\Upsilon_\pm$ would look like for a right-handed and a left-handed τ^- sample. As expected the right-handed sample peaks close to ±1 and the left-handed sample is preferably 0. It is noticeable that the left-handed distribution is more flat and the peaks at ±1 for the right-handed distribution are sharper. The peaks are not exactly at ±1 because both pions will have some non-zero energy. For simplicity these peaks will still be called peaks at ±1 for the rest of this thesis.

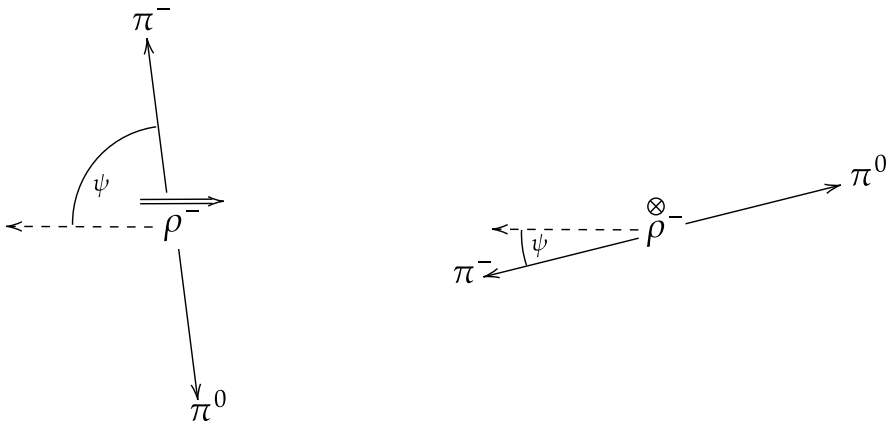

Figure 2.6: Two possible helicity configurations in the $\rho^- \to \pi^- \pi^0$ decay for different ρ^- polarisations. Solid arrows with a single line indicate flight direction, solid arrows with a double line spin orientation and $\otimes$ indicates longitudinal polarisation. The dashed arrows show the flight direction of the ρ^-. The decay angle is ψ.

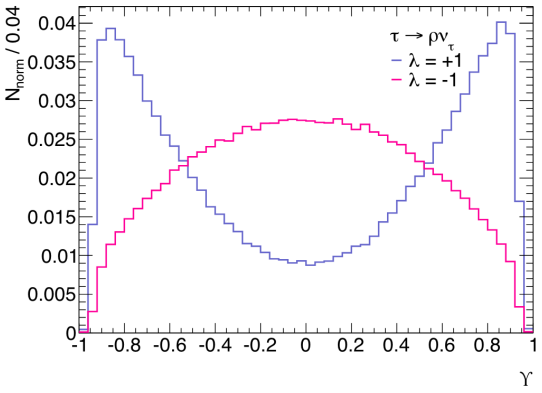

Figure 2.7: Υ distribution for a left-handed sample (pink) and a right-handed sample (blue) normalised to one. This refers to a τ^- decay [24].

2.4 Tau polarisation in Z and H decays

The particle mass is not necessarily the only property that is different for different particles. Z has spin 1 and H has spin 0. This information may not be enough to separate the particles completely in the experiment but it may help to make analyses using masses more sensitive.

The Z can decay into $\tau^+\tau^-$ via the electroweak interaction. Due to the Yukawa coupling the H interacts with fermions and can also decay into $\tau^+\tau^-$. Through $\Upsilon_\pm$ information on the τ helicities from the $Z \to \tau^+\tau^-$ and $H \to \tau^+\tau^-$ decay is available. Fig. 2.8 shows some possible decays and the resulting helicity configurations. In the H decay the τ spins need to point in opposite directions. Thus, in a back-to-back emission both τ-leptons are in the same helicity state. If the Z is polarised transversally, both τ spins point in the direction of the Z spin and thus, one τ is left-handed and the other one is right-handed. A longitudinal polarised Z will lead to a similar configuration as in the H decay which may weaken the effects analysed in this thesis.

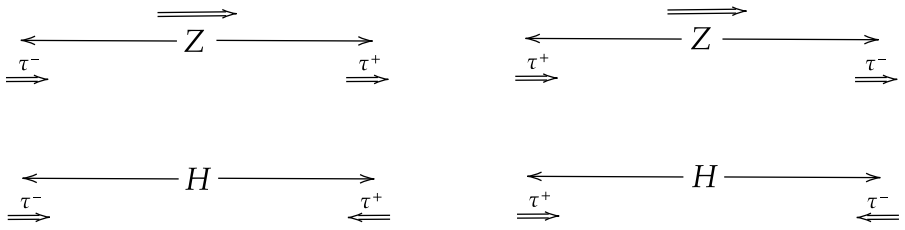

Figure 2.8: Possible helicity configurations in the $H \to \tau\tau$ and $Z \to \tau\tau$ decay. Solid arrows with a single line indicate flight direction, solid arrows with a double line spin orientation. If the Z is polarised in the other direction the τ spins are flipped. In the H decay both τ spins can be flipped. If the Z is polarised longitudinally ths situation is similar to the H decay.

It is not enough to analyse both τ from one decay separately because it is not clear which τ has which handedness. But if the correlation between both τ is analysed, differences should emerge. Because the H produces a τ^+ and a τ^- with the same helicity, one τ preferably leads to $\Upsilon_\pm = 0$ while the other one will lead to approximately $\Upsilon_\mp = \pm 1$. In the Z decay the decay products are in different helicity states. But because a τ^+ and a τ^- are produced, both τ-leptons will preferably lead to $\Upsilon_\pm = 0$ or $\Upsilon_\pm$ will be around ± 1 for both τ-leptons. However, this describes the perfect situation. In the experiment there are detector effects, decay angles, boosts, etc. that need to be taken into account. By increasing the amount of events, the $\Upsilon_\pm$ distribution can be expected to show the described effect.

2.5 Statistical sensitivity

To quantify the results and see how the sensitivity is improved using the polarisation observable, the Asimov estimate for discovery significance in counting experiments is used [25]. The median of the significance Z_0 for some signal s (H events) and background b (Z events) is

$$\text{median}[Z_0|s+b] \approx \sqrt{2((s+b)\ln(1+s/b)-s)}\,. \tag{2.3}$$

This is calculated using the likelihood ratio statistic for testing $s = 0$

$$q_0 = -2\ln\frac{L(0)}{L(\hat{s})}$$

where $\hat{s} = n - b$ is an estimator for s. L is the likelihood function (for the Poisson significance) that can be written as

$$\ln L(s) = n\ln(s+b) - (s+b) - \ln n!$$

for n observed events. Using $Z_0 \approx \sqrt{q_0}$ for sufficient large $s+b$ and $n \to s+b$ this leads to Eq. (2.3). More details can be seen in [25].

Signal and background can be split into N bins with s_i signal and b_i background events in bin i with

$$\sum_{i=1}^{N} s_i = s \quad \text{and} \quad \sum_{i=1}^{N} b_i = b\,.$$

In this case Eq. (2.3) is adapted. In q_0 the product of the likelihood function ratios for all bins is used. This leads to

$$q_0' = -2 \ln \prod_{i=1}^{N} \frac{L(0)}{L(\hat{s}_i)} \,.$$

Because the product in the logarithm can be transformed to a sum of logarithms and $\sqrt{q_0'}$ is used for the significance the median of Z_0 is calculated for multiple bins with

$$\text{median}[Z_0|\{s_i + b_i\}] \approx \sqrt{2 \sum_{i=1}^{N} ((s_i + b_i) \ln(1 + s_i/b_i) - s_i)} \,. \tag{2.4}$$

If the signal to background ratio s_i/b_i is the same for all bins Eq. (2.4) can be reduced to Eq. (2.3) using also the fact that all signal and background events in the bins have to add up to s and b and that $s/b = s_i/b_i$. For shorter notation

$$\tilde{Z}_{0,s+b} = \text{median}[Z_0|s+b] \quad \text{and} \quad \tilde{Z}_{0,\{s_i+b_i\}} = \text{median}[Z_0|\{s_i + b_i\}]$$

will be used later in this thesis.

CHAPTER 3

Experimental setup

3.1 The Large Hadron Collider

As the most powerful particle accelerator in the accelerator complex at CERN, the Large Hadron Collider (LHC) accelerates protons close to the speed of light and makes them collide at four different collision points along the 27 km long acceleration ring. At those points the detectors of the four big experiments ATLAS, CMS, A Large Ion Collider Experiment (ALICE) and Large Hadron Collider beauty (LHCb) are placed [26]. The acceleration complex is shown in Fig. 3.1.

The analysis in this thesis is based on Run 2 of the LHC (2015-2018). In this time the LHC delivered 156 fb^{-1} data at a centre of mass energy of $\sqrt{s} = 13\,\text{TeV}$ [27].

3.2 The ATLAS experiment

The ATLAS detector is, besides the CMS detector, one of the particle detectors that was used in the discovery of the Higgs boson [2, 3]. It contains multiple sub-detectors with different purposes, for example tracking detectors (inner detector) to detect tracks of charged particles. There are also calorimeters to detect electrons, photons and hadrons. Muons are usually not detected in the inner detector and the calorimeters. To measure muons a muon spectrometer is used [29–31]. An illustration of the detector can be seen in Fig. 3.2.

To describe the detector and the detected particles, a special coordinate system is used. One variable is the angle around the beam axis, the azimuthal angle ϕ. Using the polar angle θ (angle from the beam axis) the pseudorapidity $\eta = -\ln\tan(\theta/2)$ is defined. In the $\phi - \eta$ space the distance ΔR is defined as

$$\Delta R = \sqrt{\Delta\phi^2 + \Delta\eta^2}$$

using the differences in the azimuthal angle and the pseudorapidity. ΔR is used as a distance measure because differences η and ϕ are Lorentz invariant [19, 29].

In high energy particle physics experiments, the transverse momentum p_{T} is used as a kinematic variable. It is defined as the momentum that is perpendicular to the beam axis and is used because an unknown, non-negligible fraction of the momentum escapes in the beam direction [33].

In Run 2 of the LHC, a total integrated luminosity of 147 fb^{-1} was recorded by ATLAS of which

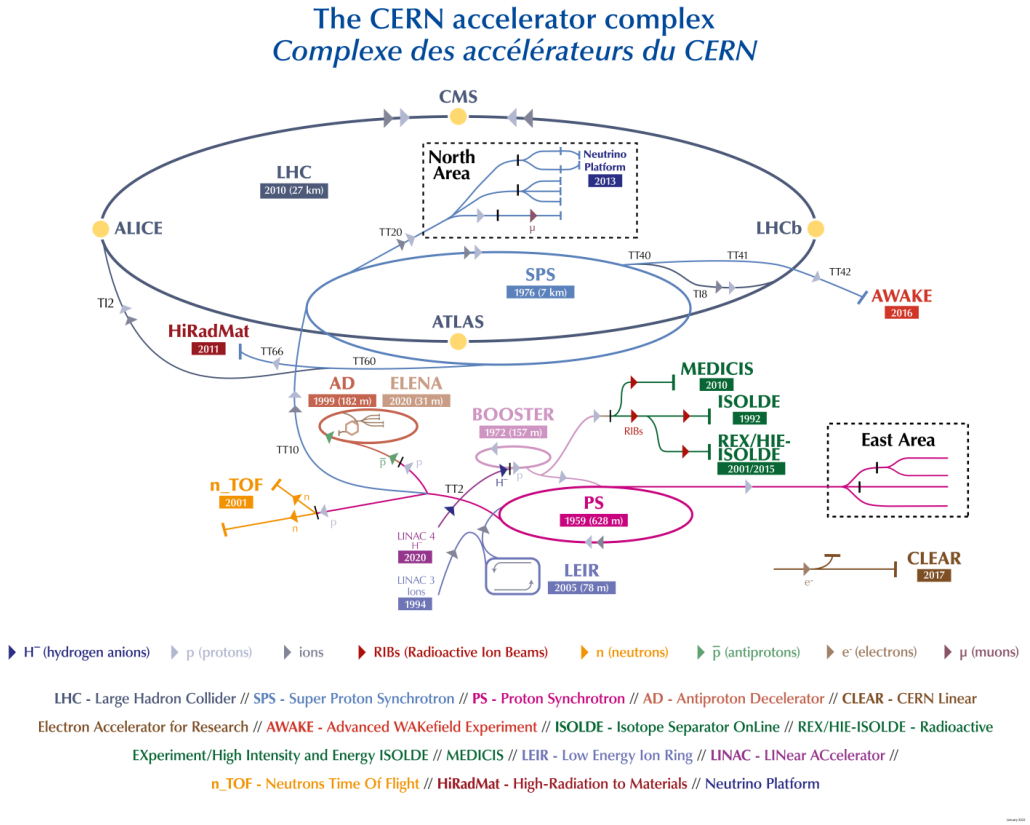

Figure 3.1: The acceleration complex and experiments at CERN [28].

139 fb^{-1} was certified for physics analysis [27]. This value is used as integrated luminosity in this thesis.

3.2.1 The Inner Detector

The Inner Detector has three main components, the Pixel Detector, the Semiconductor Tracker and the Transition Radiation Tracker, that are immersed in a 2 T magnetic field parallel to the beam. With them, it is possible to measure the direction, momentum and charge of charged particles passing through the Inner Detector. The Pixel Detector is the closest detector to the beam line. Particles from the collision leave a small amount of energy in some of the many silicon pixels. This detector has the highest precision (almost 10 µm). With the Semiconductor Tracker particle tracks can be measured with a precision of up to 25 µm. To do this, the detector is built such that a particle crosses at least four silicon layers when passing through the tracker. The last layer, the Transition Radiation Tracker, is built around the other two sub-detectors. It is made up of tubes containing a gas mixture and a gold-plated tungsten wire in its centre. Particles can ionise the gas and create an electric signal that helps to identify the particle type [20, 34].

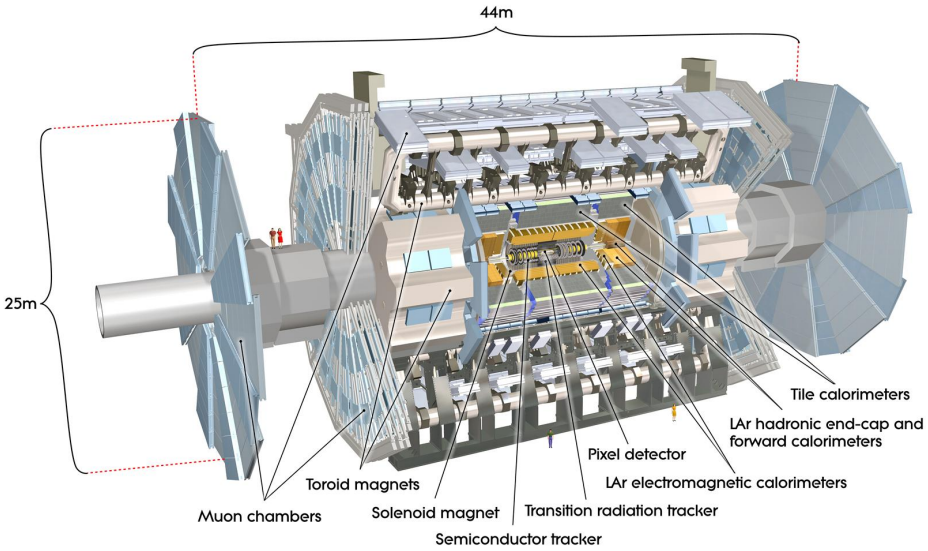

Figure 3.2: Illustration of the ATLAS detector. Opened parallel to the beam axis to see the insides [32].

3.2.2 Calorimeters

There is an electromagnetic and a hadronic calorimeter in the ATLAS detector, that is used to detect electrons, photons and hadrons and measure their energy. The electromagnetic calorimeter uses lead as an absorber to convert the incoming particle into a shower of low energy particles, which ionise liquid argon to produce an electric current. This current can be measured. The electromagnetic calorimeter is separated into different layers in the central rapidity region. The innermost layer is optimised for γ/π^0 separation. Electron and photon showers leave energy in the calorimeter. Most of this energy is collected in the second layer. A last layer corrects leakages beyond the calorimeter [20, 35].

The hadronic calorimeter uses scintillator tiles ($|\eta| < 1.7$) or liquid argon ($1.5 < |\eta| < 4.9$) as active media. Steal, copper or tungsten is used as absorber [20].

3.3 Tau reconstruction

The details of the τ reconstruction are shown in [20] but will be summarised here. A hadronic τ decay produces a jet. The measurements from the calorimeters are used as input for the anti-k_t algorithm [36] to build jets. The Inner Detector tracks are matched with τ candidates, if they fulfil certain criteria for their p_{T} ($p_{\mathrm{T}} > 1$ GeV), the number of hits (at least two in the pixel layer and seven in the pixel and silicon microstrip layer) and on the distance of closest approach of the track and the primary vertex of the τ candidate ($|d_0| < 1$ mm (transverse plane) and $|z_0 \sin\theta| < 1.5$ mm (longitudinally)). Adding up the charge of all matched tracks determines the charge of the τ [20].

The τ candidates need to be separated from background, that originates from other jets that can be initiated by quarks and gluons. Using the shower shape and tracking information in a multivariate algorithm a τ jet is discriminated from the background jets.

This thesis focuses on the 1p1n decay mode and thus, a charged hadron ($\pi^{\pm}$) and a π^0 have to be measured and reconstructed. The τ decay products are reconstructed using the Tau Particle Flow [20], resulting in so-called charged and neutral particle flow objects. The latter is used for the neutral pion. The π^0 decays mostly into a pair of photons. Half of these photons convert into $e^- e^+$ because of interactions with beam pipe or Inner Detector material. The π^0 is reconstructed from the photon energy deposit in the electromagnetic calorimeter and thus, the energy is available for the calculation of $\Upsilon_{\pm}$. The energy deposit has to be disentangled from the charged hadron shower. A $\pi^{\pm}$ has a sufficiently long lifetime to always reach the calorimeter, where it decays in a cascade of hadronic interactions and can be reconstructed as a cluster of hadronic energy deposits. To determine the $\pi^{\pm}$ momentum, and thus its energy, the tracking system (Inner Detector) is sufficient. The tracker is also more performant in the analysed momentum range. The $\pi^{\pm}$ energy can be subtracted from the total energy measurement of the corresponding clusters, leaving only neutral particle clusters. They can be identified with the π^0 decay products [20].

CHAPTER 4

Ditau channel Z and H decay data

4.1 Event generation

In this thesis Monte Carlo (MC) simulated events for $H \rightarrow \tau\tau$ and $Z \rightarrow \tau\tau$ processes are provided [8]. For the analysis the integrated luminosity is set to 139 fb^{-1} to fit the recorded ATLAS data in Run 2 of the LHC [27]. The Z events are generated with the Sherpa 2.2.1 generator. For QCD production of Z + jets the simulation uses next-to-leading-order (NLO) matrix elements for up to two partons. For up to four partons and the electroweak production LO matrix elements are used [8].

At LHC the main production mode for a SM H is ggF with a cross section of 48.61 pb at a centre of mass energy of $\sqrt{s}$ = 13 TeV [37]. This thesis uses SM H simulated events with ggF as production mode. The most relevant production mode after ggF is vector-boson fusion. This thesis uses only ggF H events without limiting the results with regard to vector-boson fusion. The analysis works analogously for vector-boson fusion H data. The matrix element simulation is performed with Powheg Box v2 and the decays with Pythia 8. For QCD the simulation accuracy is next-to-next-to-leading-order (NNLO). For electroweak corrections the LO is used [8].

The sample contains truth (matrix element simulation) and reconstructed data for both τ-leptons. Truth data is only available if two τ-leptons were reconstructed. Thus, there is a bias for truth data with no further information that must be kept in mind. Based on this, three cases are analysed in this thesis:

1. truth: The truth data, including the truth decay mode, is used for the analysis.
2. d matched: The reconstructed data is used and the reconstructed decay mode has to match the truth decay mode.
3. reco: the reconstructed data, including the reconstructed decay mode, is used.

The reco case is the closest to the data that is collected in the experiment and thus, the most interesting one.

4.2 Event selection

Multiple cuts are applied to the events that are discussed in this section. There are some necessary cuts. The charge is reconstructed by adding up the curved tracks, with different signs for different

curvature directions, in the Inner Detector. Having the wrong number of curved tracks or, for example, measuring the opposite curvature can lead to charges with $|Q| \neq 1$. Because τ-leptons have $|Q| = 1$, these events are ignored. To conserve charge another constraint is that the two reconstructed τ-leptons have opposite charge. Thus, the Q cut

$$\left(|Q_{\tau_0}| = 1\right) \wedge \left(|Q_{\tau_1}| = 1\right) \wedge \left(Q_{\tau_0} \cdot Q_{\tau_1} = -1\right)$$

is applied. In this notation τ_0 and τ_1 correspond to the leading (higher p_T) and sub-leading (lower p_T) τ-leptons.

The simulated data contains different hadronic τ decay modes. Because the observable $\Upsilon_\pm$ works for $\tau^\pm$ decays that produce a charged hadron ($\pi^\pm$) and a π^0 the decay mode d cut

$$d = \mathrm{1p1n}$$

is required.

In the analysis of some kinematic variables (especially in p_T and invariant mass distributions) some outliers were observed. An example is shown in Fig. 4.1 with an outlier above 100 GeV for the leading jet p_T. This only occurs in the Z data and is caused by some few events with high negative MC weights. These events are considered to be non-physical and are ignored using the cut

$$|\mathrm{weight}_{\mathrm{MC},Z}| < 50\,.$$

The exact cause of this problem is unknown. With this cut approximately eleven events are lost with MC weights that have a magnitude of 10^2. Usually, the sum of weights has to be corrected. However, as the loss is only approximately 0.005 % of the sum of weights this loss is negligible. This cut is consistently applied in the analysis below.

There are cuts that are used in the H analysis [8] and will also be applied here. These cuts are described below. Some of these cuts are motivated by improving the analysis, others are necessary due to constraints given by the detector and the triggers. Triggers are necessary to preselect data to a manageable level. The level-1 trigger is located on the detector and decides whether an event is interesting enough to retain in less than 2.5 µs. The next, higher-level trigger is implemented on a large CPU farm and reduces the amount of data by analysing each collision event in 200 µs. This system reduces the amount of data significantly to about 1000 events per second that are used in the offline analysis [38]. Not all detector and trigger constraints are part of the simulation and thus they are necessary to obtain similar results as with real data. The distribution of the variable that is used for the currently discussed cut is shown in Appendix A as a logarithmic and in Appendix B as a normalised histogram for all three cases. For these histograms the cuts discussed so far are applied.

The used data already has some p_T cuts on the τ-leptons. But there are still cuts that need to be applied in the analysis. To ensure the fit of the recorded and the simulated data, operation at the trigger's efficiency plateau is necessary. Therefore, the cuts

$$p_{\mathrm{T},\tau_0} > 40\,\mathrm{GeV} \quad \text{and} \quad p_{\mathrm{T},\tau_1} > 30\,\mathrm{GeV}$$

are applied. Figure B.1 and Fig. B.2 show that the H data dominates at higher p_T, because SM H data is used and the SM H has a higher mass than Z. For a potential BSM H at lower masses this may change. However, if this BSM H is produced with ggF the probability for some (recoil) QCD jets is

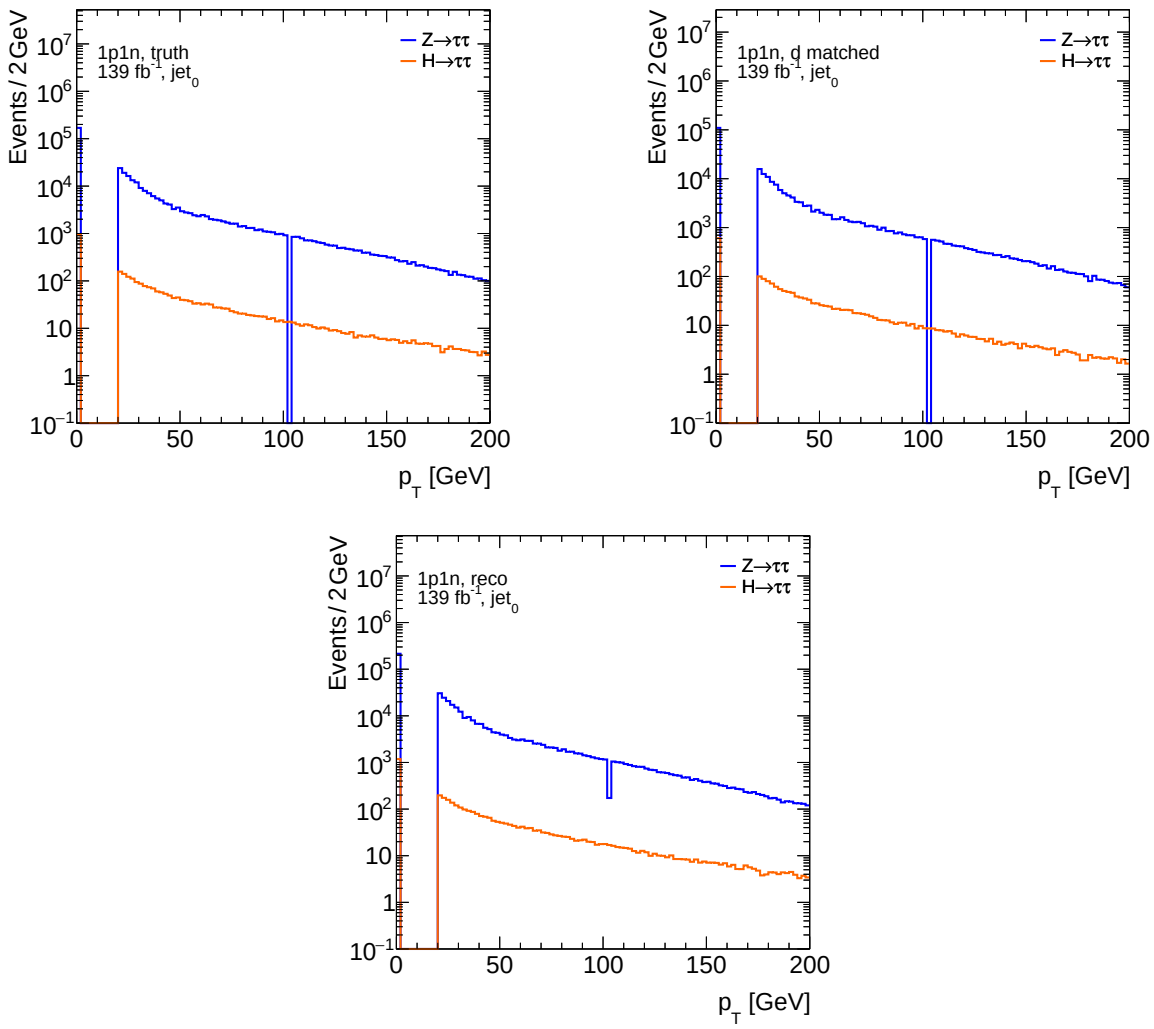

Figure 4.1: Leading jet (jet$_0$) p_{T} with an outlier above 100 GeV. LHC Run 2 data is used (simulated ATLAS $Z \to \tau\tau$ and $H \to \tau\tau$ events). A Q and d cut are applied on both samples and a MC weight cut on the Z sample.

higher than in the Z production. Therefore, the H will probably be more boosted than the Z, which may cause differences in these p_{T} distributions.

In order to operate on the trigger's efficiency plateau, it is further necessary that the leading jet jet$_0$ has

$$p_{\mathrm{T,\,jet_0}} > 70\,\mathrm{GeV}\,.$$

This value is higher than for the τ-leptons because jets are reconstructed at the level-1 trigger and not at the higher-level triggers. There is a lower E_{T} threshold of 25 GeV at the level-1 trigger. This can differ significantly from the offline reconstruction which causes this p_{T} bound to be this high at

70 GeV. Because this level-1 trigger has an upper bound for η for jets, the cut

$$|\eta_{\text{jet}_0}| < 3.2$$

is applied.

Another necessary cut, due to some trigger-level cut, is

$$\Delta R_{\tau\tau} < 2.5\,.$$

The motivation for this cut can be seen in Fig. B.3. For low $\Delta R_{\tau\tau}$ the H data dominates. By cutting the part where Z dominates, the analysis is improved. This cut (with 2.8 instead of 2.5) is implemented in the trigger which makes this cut necessary. For this variable there is also a lower bound

$$\Delta R_{\tau\tau} > 0.6$$

to make sure the τ candidates at the level-1 trigger don't have overlapping cores.

Besides the jets from the τ decays, multiple QCD jets can form. To improve the selection of jets that are produced from a τ decay, the cut

$$|\Delta\eta_{\tau\tau}| < 1.5$$

is applied. QCD jets do not originate from resonances and are distributed over the entire solid angle. The τ decay jets will be closer together and thus, this cut helps to select real τ-leptons.

The selection of real and rejection of fake τ-leptons can be further improved by a recurrent neural network that analyses the data that is used for the reconstruction. If only τ-leptons are used that are identified as "medium" by the network, 25 % of real τ-leptons but many of the fake τ-leptons are lost. This only works for 1p decays [20, 39].

Using all the described cuts together will be called analysis cut in the analysis below. However, for a SM H analysis, one powerful variable is the invariant mass. To get an idea how the analysed polarisation observable can improve a SM H analysis the invariant mass will also be used in an extra analysis step. Because of the missing transverse energy due to the neutrino, the invariant mass from the four-vectors of the τ-leptons will not lead to the particle masses of H or Z. In order to obtain the invariant mass, the Missing Mass Calculator (MMC) is used [40]. Figure B.9 shows that the H data becomes dominant at approximately 110 GeV. As a cut an approximately symmetric range around the SM H mass is used and thus, the cut

$$110\,\text{GeV} \leq m_{\tau\tau}^{\text{MMC}} \leq 140\,\text{GeV}$$

is applied where $m_{\tau\tau}^{\text{MMC}}$ is the mass from the MMC. The analysis cut in connection with this mass cut will be called analysis cut + MMC below.

To get an idea how these cuts affect the data and how many events are left after the cuts the cutflow for the reconstructed data is shown in Table 4.1. As expected and in accordance with the described cuts and the distributions in Appendix A and Appendix B, there are cuts ($m_{\tau\tau}^{\text{MMC}}$, $p_{\text{T},\tau_{0,1}}$ and $p_{\text{T,jet}_0}$) that favour H data and will improve the analysis. Other cuts do not really favour Z or H. The percentages for each cut change if the order in which the cuts are applied changes, but the basic effect of the cuts stays. The resulting number of available events after applying all cuts does not change.

Table 4.1 shows that the analysis cut reduces the number of Z events to 0.8 % and the number of H events to 1.8 %. These percentages differ because of the H favouring cuts. If the analysis cut + MMC is used, this drops to 0.1 % for the Z and 1.2 % for the H because the $m_{\tau\tau}^{\text{MMC}}$ was chosen around the SM H mass.

Table 4.1: Cutflow for reconstructed Z and H data showing number of events, percentage of remaining events compared to no cut (abs) and to the combined previous cuts (rel).

Cut	Z events	abs / %	rel / %	H events	abs / %	rel / %
No cut	2 494 893	100.0	100.0	21 361	100.0	100.0
$Q_{\tau_0} = \pm 1, Q_{\tau_1} = \mp 1$	1 980 398	79.4	79.4	17 192	80.5	80.5
$d_{\tau_0} = \text{1p1n}, d_{\tau_1} = \text{1p1n}$	474 811	19.0	24.0	4 023	18.8	23.4
$p_{\text{T},\tau_0} > 40\,\text{GeV}, p_{\text{T},\tau_1} > 30\,\text{GeV}$	240 632	9.6	50.7	3 059	14.3	76.0
$p_{\text{T,jet}_0} > 70\,\text{GeV}$	34 624	1.4	14.4	704	3.3	23.0
$\lvert\eta_{\text{jet}_0}\rvert < 1.5$	33 886	1.4	97.9	679	3.2	96.5
$0.6 < \Delta R_{\tau\tau} < 2.5$	31 107	1.2	91.8	618	2.9	91.0
$\lvert\Delta\eta_{\tau\tau}\rvert < 1.5$	30 300	1.2	97.4	584	2.7	94.5
Identification “medium”	20 440	0.8	67.5	386	1.8	66.1
$110\,\text{GeV} < m_{\tau\tau}^{\text{MMC}} < 140\,\text{GeV}$	2 139	0.1	10.5	255	1.2	66.2

CHAPTER 5

Analysing τ polarisation in Z and H decays

In this chapter the polarisation observable introduced in Section 2.3.1, using the events discussed in Chapter 4, is analysed. The analysis will cover three different cuts on the data. At first only the Q and d cut (and the MC weight cut on the Z data) is applied. After that the analysis cut described in Chapter 4 is used followed by the analysis cut + MMC. This gives an overview on how the cuts affect the data and the sensitivity of the analysis. For every cut the three cases truth, d matched and reco are analysed.

5.1 Charged energy asymmetry correlation

As discussed in Section 2.4 analysing $\Upsilon_\pm$ for only one τ in the H and Z decay is not sufficient. Therefore, a two-dimensional histogram for Υ_+ and Υ_- is created. Figure 5.1 shows the histograms for Z and H in the different cases if only the Q and d (and the MC weight for Z) cut are applied.

The shapes of the histograms are as expected. As discussed in Section 2.4 for Z it is expected that Υ_+ and Υ_- both peak at ±1 or both peak at 0. Because the peaks at ±1 are sharper, these are the ones clearly visible in Fig. 5.1. For H, $\Upsilon_\pm$ can be expected to peak at ±1 while $\Upsilon_\mp$ peaks at 0. Figure 2.7 indicates that the distribution that should peak at 0 resembles a flat distribution, rather than a sharp peak. This leads to the circular structure for the H sample in Fig. 5.1.

The edges of the distributions in Fig. 5.1 show hardly any events. This can also be seen in Fig. 2.7. The reason for this is that the pions used to calculate $\Upsilon_\pm$ will have some non-zero energy (their mass and some energy so they can be detected), so $\Upsilon_\pm$ cannot be exactly ±1.

Another effect that is observed in Fig. 5.1 is an asymmetry in the histogram. There are more events around $\Upsilon_\pm = -1$ than around $\Upsilon_\pm = +1$. This effect cannot be explained reasonably for the truth case because of the above-mentioned bias in the truth data. For the reco and d matched case, an efficiency ε graph is created. To obtain this graph, $\Upsilon_\pm$ is calculated with truth data but with the cut that the reconstructed and the truth decay mode match. This histogram is divided by $\Upsilon_\pm$ calculated with truth data and only the truth decay mode. The resulting graph in Fig. 5.2 gives an idea on how efficient the decay mode reconstruction is. The efficiency is significantly reduced for $\Upsilon_\pm \to +1$ which could explain the asymmetry in the reco and d matched case. The efficiency drops for $\Upsilon_\pm \to +1$ because in this case the neutral pions have a very low energy which makes it harder to detect them. Thus, the probability increases that the reconstruction assigns the 1p0n instead of the 1p1n decay mode to an

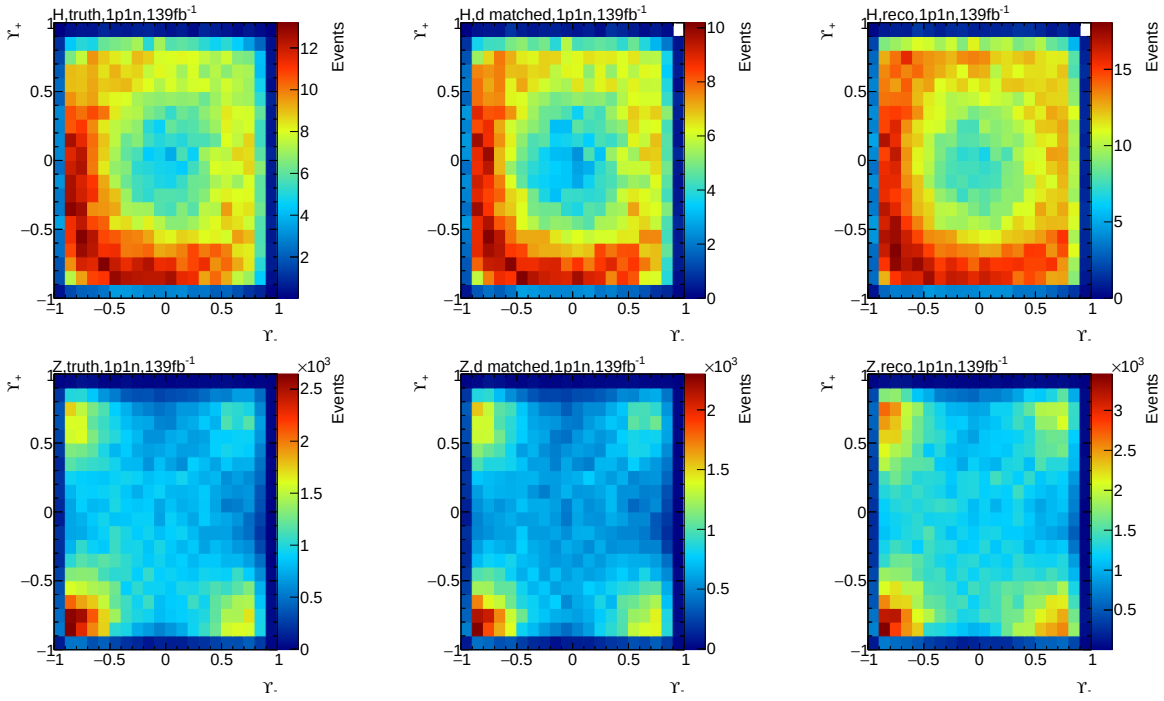

Figure 5.1: $\Upsilon_+\Upsilon_-$ correlation for H (top) and Z (bottom) events with a Q and d cut applied on both samples and a MC weight cut on the Z sample. LHC Run 2 data is used (simulated ATLAS $Z \rightarrow \tau\tau$ and $H \rightarrow \tau\tau$ events).

event that is actually a 1p1n decay. The efficiency doesn't drop for $\Upsilon_\pm \rightarrow -1$ because one charged hadron in the decay products is required and charged hadrons can be detected with the tracker.

The shapes of the two-dimensional histograms have no big differences when the truth, d matched and reco case are compared. The shape seems to be slightly more clearer in the truth and d matched case than in the reco case but in every case the difference between Z and H is visible.

As a next step the analysis cut is applied. The resulting two-dimensional histograms are shown in Fig. 5.3. The number of events gets much lower which is expected from the cutflow in Table 4.1. The four peaks in the Z histograms and the circular structure in the H histograms are still visible. In Fig. 5.1 a structure between the Z peaks can be seen. This is visible in the truth case after the analysis cut but vanishes in the d matched and reco case. The structure in the H histograms is still visible after the analysis cut but less smooth than in Fig. 5.1 due to the reduced number of events. The low event edges and the asymmetry of the histograms remain.

In a last step the analysis cut + MMC is applied. The resulting histograms are shown in Fig. 5.4. The H histograms have slightly less events but are still similar to Fig. 5.3. In the Z histograms many events are lost and the structure that is observed for the other cuts is less present. Less events are expected and this also causes some losses in the structure. Another problem is one bin with around 30 events in all Z histograms with the analysis cut + MMC that distorts the scale.

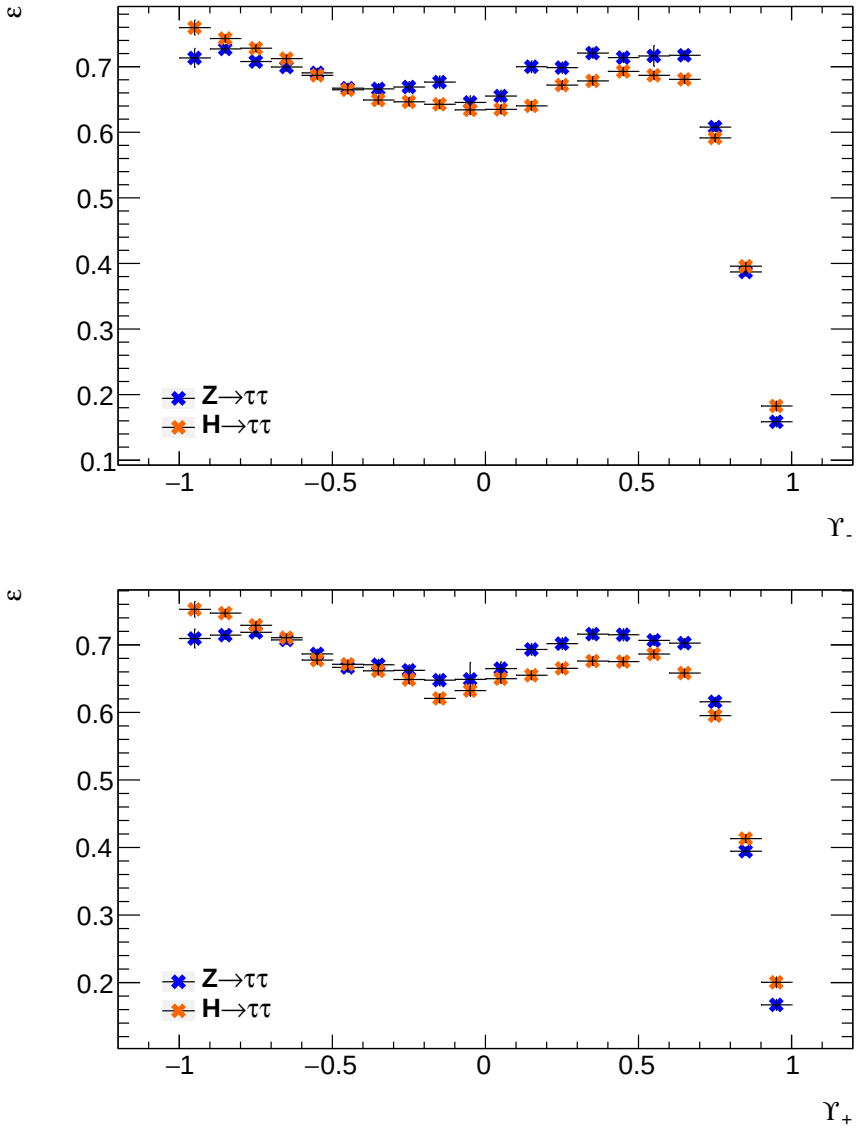

Figure 5.2: Decay mode reconstruction efficiency for different $\Upsilon^{\pm}$. Truth data is used and the histogram that requires the truth and reconstructed decay mode to match is divided by the histogram that only uses the truth decay mode. Also the Q and d cut (and the MC weights cut on the Z sample) are applied. LHC Run 2 data is used (simulated ATLAS $Z \to \tau\tau$ and $H \to \tau\tau$ events).

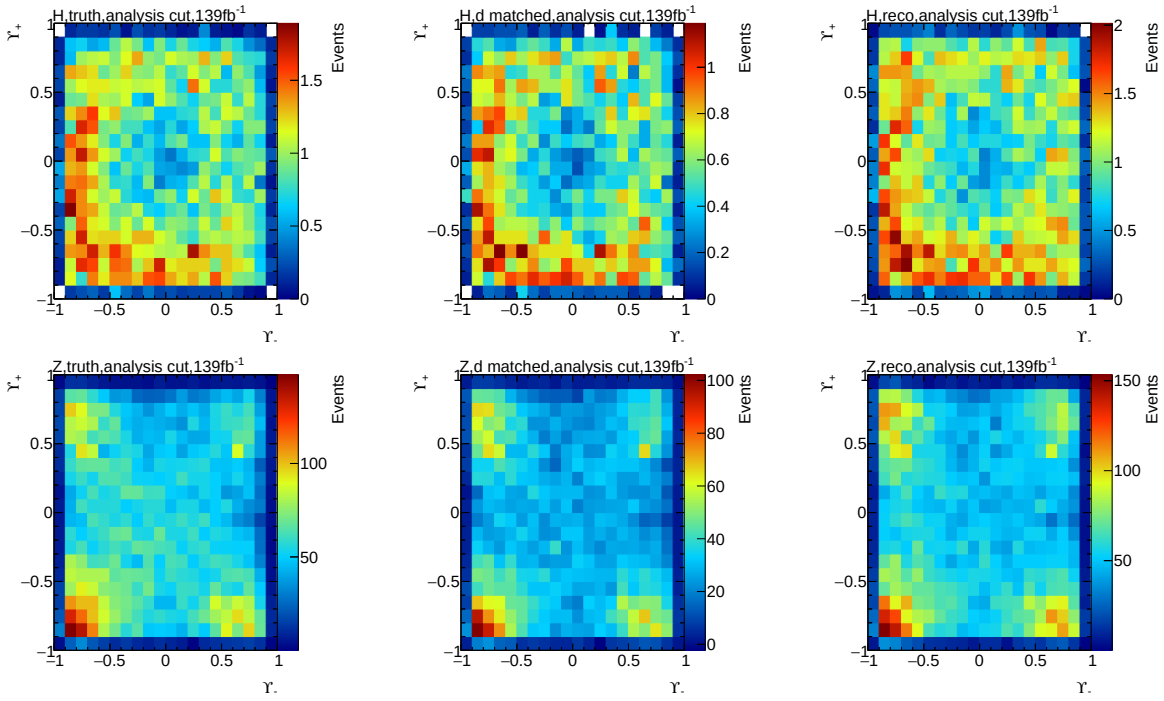

Figure 5.3: $\Upsilon_+\Upsilon_-$ correlation for H (top) and Z (bottom) events with the analysis cut applied on both samples. LHC Run 2 data is used (simulated ATLAS $Z \to \tau\tau$ and $H \to \tau\tau$ events).

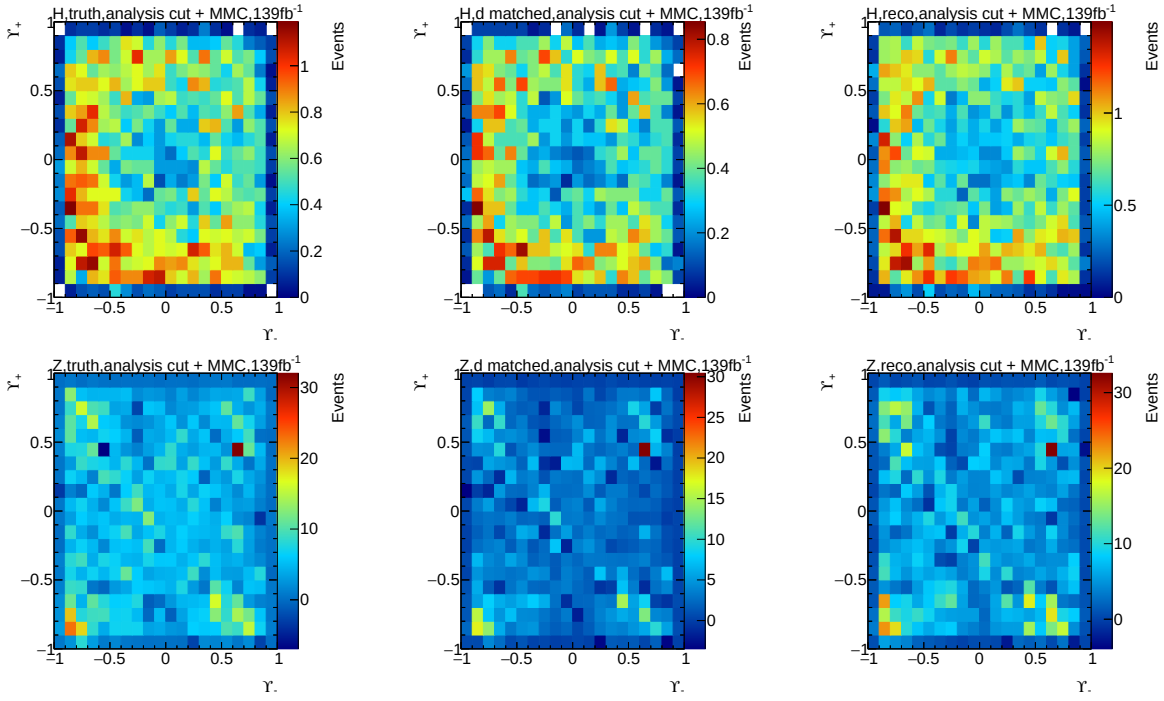

Figure 5.4: $\Upsilon_+\Upsilon_-$ correlation for H (top) and Z (bottom) events with the analysis cut + MMC applied on both samples. LHC Run 2 data is used (simulated ATLAS $Z \to \tau\tau$ and $H \to \tau\tau$ events).

5.2 Projection into one dimension

The two-dimensional histograms contain many bins and especially in the analysis cut and analysis cut + MMC there are some bins with only few events. The absence of background events in a bin leads to problems when calculating the sensitivity described in Section 2.5. Also the H histograms may not be smooth enough and there may not be enough statistics to use a neural network. To analyse the sensitivity of the polarisation observable, the $\Upsilon_+\Upsilon_-$ correlation information is projected into one dimension. From multiple tested projection functions a manual selection of different areas of the two-dimensional histograms above is the most sensitive. The function

$$A_b(\Upsilon_+, \Upsilon_-) = \begin{cases} 1, & \text{if } \Upsilon_- \leq -b \wedge \Upsilon_+ \leq -b \\ 2, & \text{if } \Upsilon_- \geq b \wedge \Upsilon_+ \geq b \\ 3, & \text{if } (\Upsilon_- \geq b \wedge \Upsilon_+ \leq -b) \vee (\Upsilon_- \leq -b \wedge \Upsilon_+ \geq b) \\ 4, & \text{if } |\Upsilon_-| \leq b \wedge |\Upsilon_+| \leq b \\ 5, & \text{if } (|\Upsilon_-| < b \wedge |\Upsilon_+| > b) \vee (|\Upsilon_-| > b \wedge |\Upsilon_+| < b) \end{cases}$$

assigns a number to different areas in the two-dimensional histograms. The choice of the parameter $b \in [-1, 1]$ will be optimised later in this thesis to maximise sensitivity. An example on how the numbers are assigned to different areas is shown in Fig. 5.5 for $b = 0.5$ for a Z histogram. Because of the symmetry the lower right and upper left areas are assigned the same number.

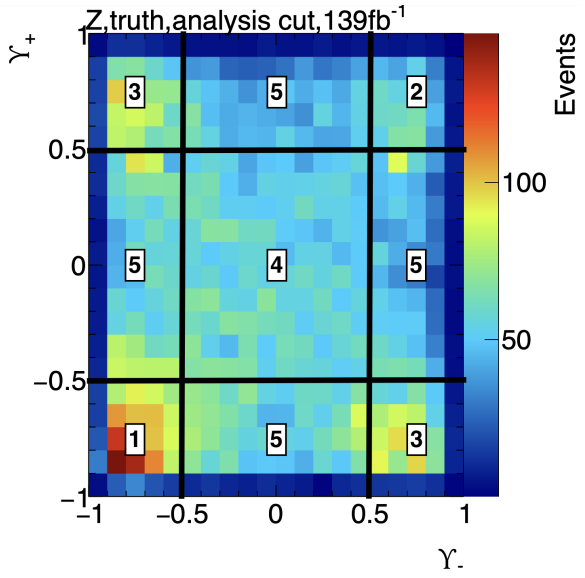

Figure 5.5: Example for the assignment of numbers to different areas in the $\Upsilon_+\Upsilon_-$ correlation histograms using $A_b(\Upsilon_+, \Upsilon_-)$ with $b = 0.5$.

5.2.1 Optimisation of the projection

The projection function $A_b(\Upsilon_+, \Upsilon_-)$ has b as parameter that can be chosen in the interval $[-1, 1]$. To optimise this parameter the significance is calculated with Eq. (2.4) for different b. Because it is the most relevant case, this optimisation is done for the reco case. The result is shown in Fig. 5.6. In this case $A_b(\Upsilon_+, \Upsilon_-)$ is most sensitive for $b = 0.5$. The optimal choice for b is close to 0.5 for all different cases. Looking at Fig. 5.5 or the two-dimensional histograms shown above, this parameter choice isolates the Z peaks and is around the border of the circular structure in the H histograms. Thus, $b = 0.5$ is also a logically reasonable choice.

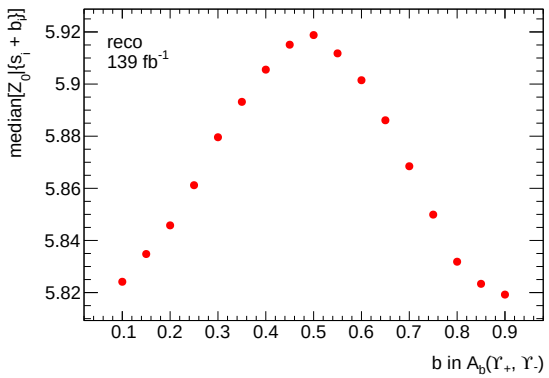

Figure 5.6: Significances, calculated with Eq. (2.4), for different b in $A_b(\Upsilon_+, \Upsilon_-)$ for the reco case with the Q and d cut applied.

5.2.2 Shape of the projection

Figure 5.7 shows the shape of $A_{0.5}(\Upsilon_+, \Upsilon_-)$ for different cuts. The H is more present in area 5 because of its circular structure in the two-dimensional histograms. The other areas are harder to distinguish, but because the H is more present in area 5 the Z dominates in the other areas. By applying different cuts the shape changes slightly, but the overall shape differences remain. Because for the used SM H the p_T cuts favour the H, the analysis cut without these cuts is also analysed but no big changes in the shape are observed. Figure 5.8 shows that in the π^0 reconstruction for high transverse energies the relative transverse energy resolution is flat and low and the relative transverse energy linearity is around 1 and flat [20]. This explains that there is no loss in shape when applying the analysis cut. Applying the analysis cut + MMC also has no remarkable impact on the shapes. For reasons of clarity and because no further information is gained this cut is not shown in Fig. 5.7.

5.3 Results

Figures 5.9 to 5.11 show $A_{0.5}(\Upsilon_+, \Upsilon_-)$ for the different cuts and cases discussed above as a stacked histogram of Z and H events. To see the H events Appendix C also shows $A_{0.5}(\Upsilon_+, \Upsilon_-)$ but on a logarithmic scale, without errors and H and Z swapped. The errors in Figs. 5.9 to 5.11 are the Poisson errors of signal and background together. Because of the number of background events the H events

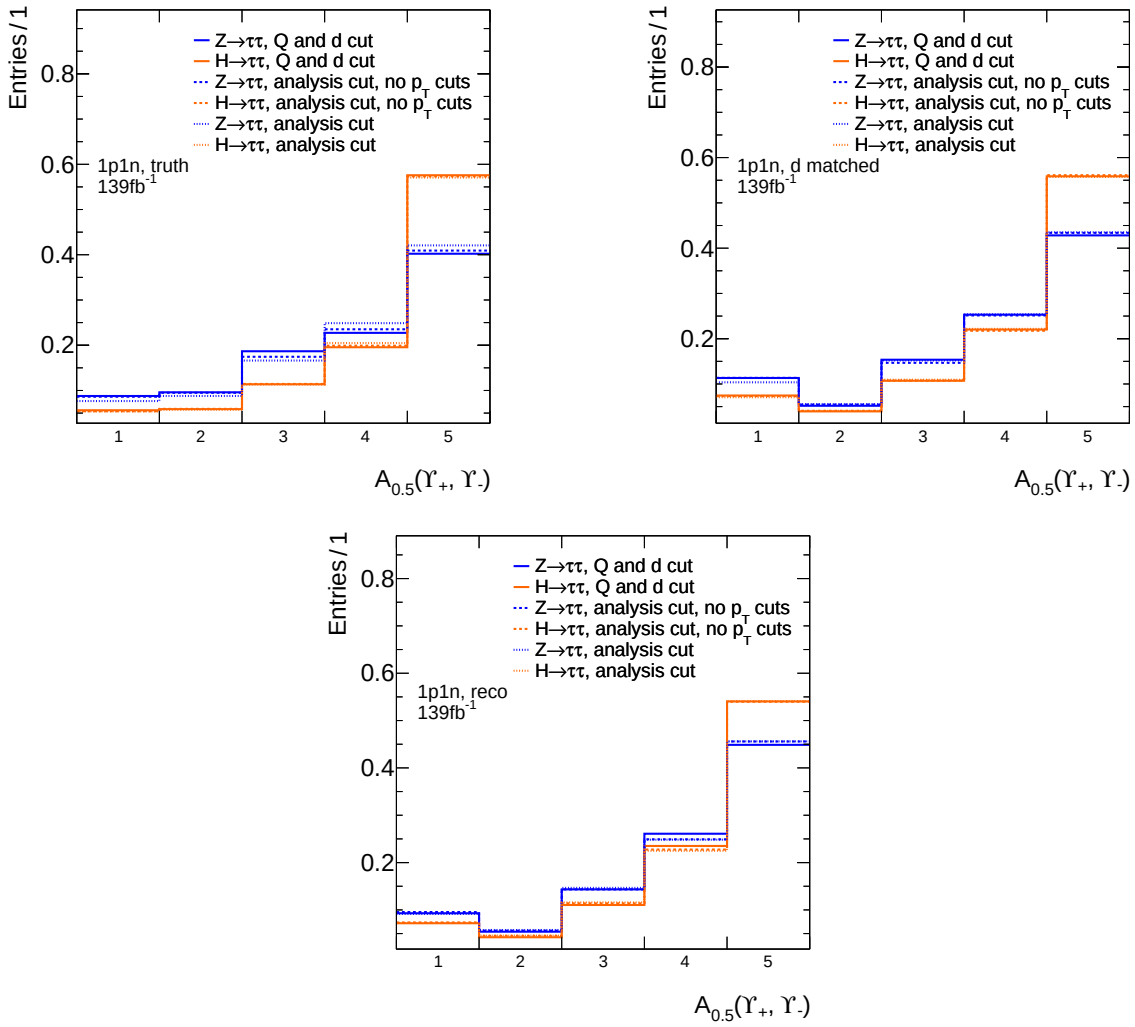

Figure 5.7: Shapes of $A_{0.5}(\Upsilon_+, \Upsilon_-)$ for H and Z for different cuts. The histograms are normalised to 1. LHC Run 2 data is used (simulated ATLAS $Z \to \tau\tau$ and $H \to \tau\tau$ events).

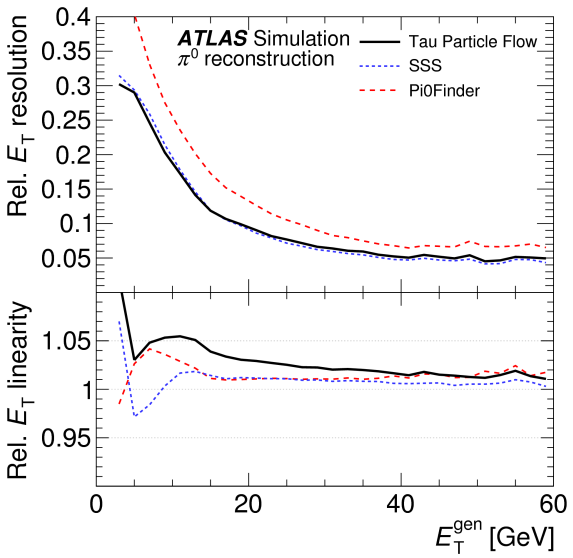

Figure 5.8: Resolution and linearitiy of the reconstruction candidate π^0 transverse energy as a function of the generated π^0 transverse energy [20].

are only visible for bin 5 in the Q and d cut histogram in Fig. 5.9. This is the area where the shape difference is strongest and the bin with most H events.

After applying the analysis cut there are less events and the H events are somewhat favoured. The H events are more visible in Fig. 5.10, especially in bin 5 and 4. The differences in the other bins are still very small. Because there are less events, the relative error increases and thus, the error bars are visible. The signal in bin 5 is stronger than the error and in the other bins the error is of the order of the signal or even bigger.

When also the $m_{\tau\tau}^{\text{MMC}}$ cut is applied, many background events are rejected and thus, the H events are more present in Fig. 5.11 in every bin. Because events are lost, the relative error increases again. In bin 3, 4 and 5 the signal is stronger than the error and in bin 1 and 2 the signal is about as large as the error.

To see how sensitive $A_{0.5}(\Upsilon_+, \Upsilon_-)$ is, the significance is calculated with Eq. (2.4). As a comparison to see how the sensitivity is improved, a constant signal to background ratio for each bin is assumed. In this case Eq. (2.3) can be used to calculate the significance where all background events are summed up to b and all signal events to s. The difference between the values from Eq. (2.4) and Eq. (2.3) is used as a metric how much sensitivity is gained with $A_{0.5}(\Upsilon_+, \Upsilon_-)$. The significances are shown in Table 5.1. The sensitivity is improved in all cases. The significances drop when the analysis cut is applied due to the loss of many events. As shown above the shape of the distribution does not really change for this cut and thus, the significance drop is a result of the reduction of the number of analysed events. The significances increase for the analysis cut + MMC because of the background rejection in this cut. The truth cases have the biggest improvements but, as mentioned above, the truth data has a bias that cannot be taken into account. The significances in the d matched case are lower than in the reco case due to less events. But the sensitivity gained is higher in the d matched than the reco case. This is because the d matched case also uses the truth decay mode information that is not available when only reconstructed data is used. In the reco case events with incorrectly assigned decay modes

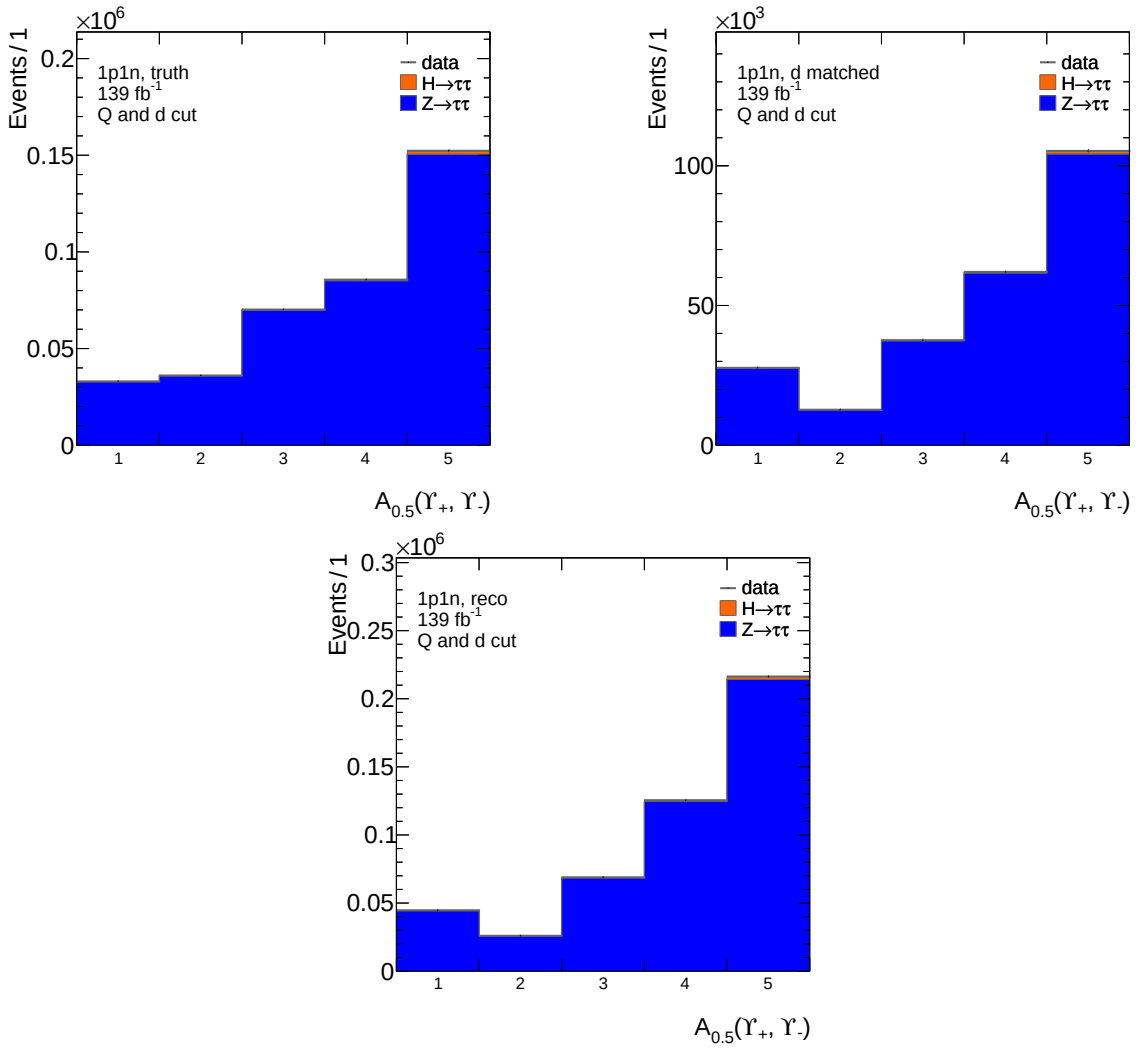

Figure 5.9: $A_{0.5}(\Upsilon_+, \Upsilon_-)$ for the Q and d cut for the three different cases. H and Z are stacked and the errors are the Poisson errors for the events of both particles together. LHC Run 2 data is used (simulated ATLAS $Z \rightarrow \tau\tau$ and $H \rightarrow \tau\tau$ events).

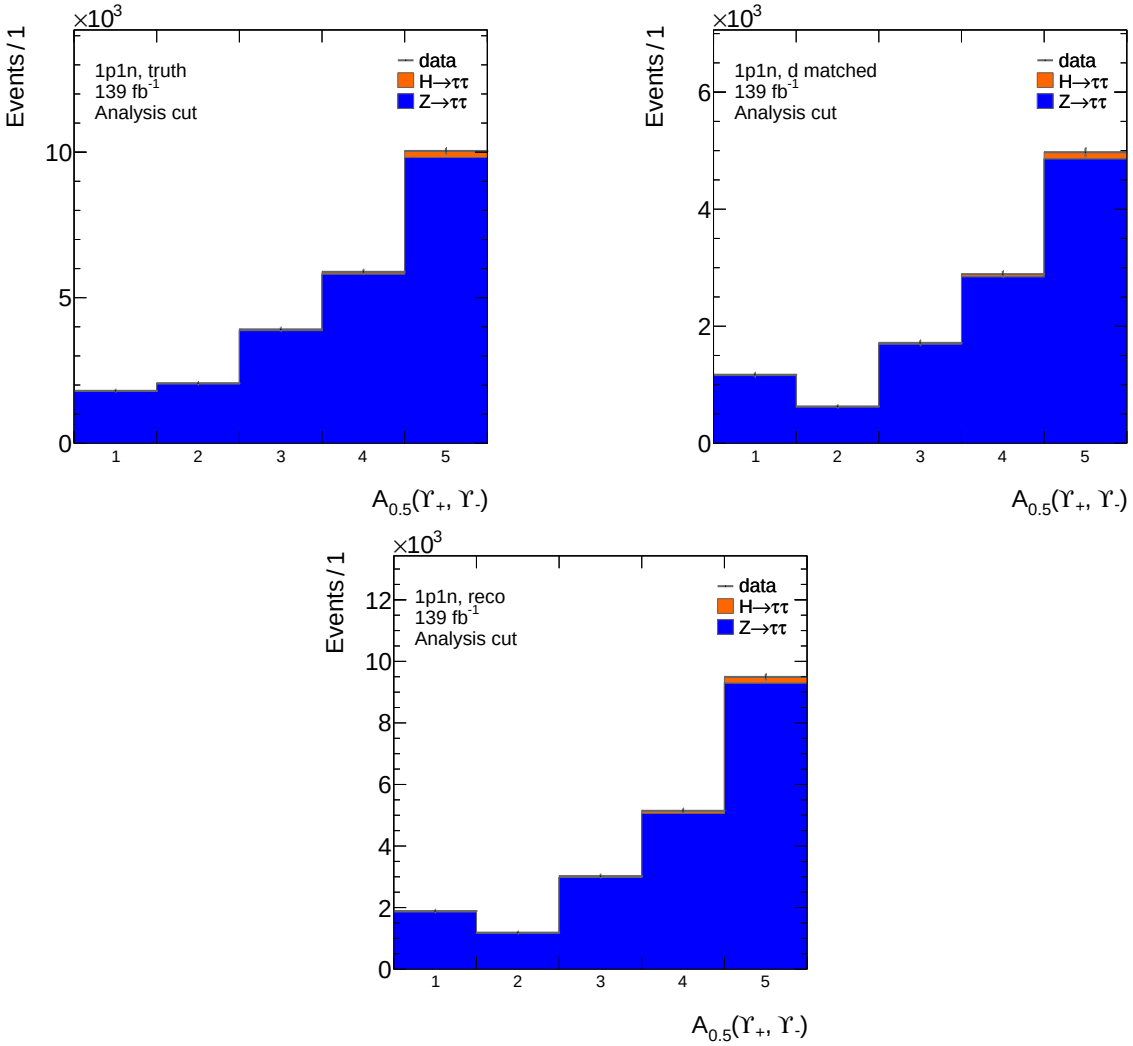

Figure 5.10: $A_{0.5}(\Upsilon_+, \Upsilon_-)$ for the analysis cut for the three different cases. H and Z are stacked and the errors are the Poisson errors for the events of both particles together. LHC Run 2 data is used (simulated ATLAS $Z \to \tau\tau$ and $H \to \tau\tau$ events).

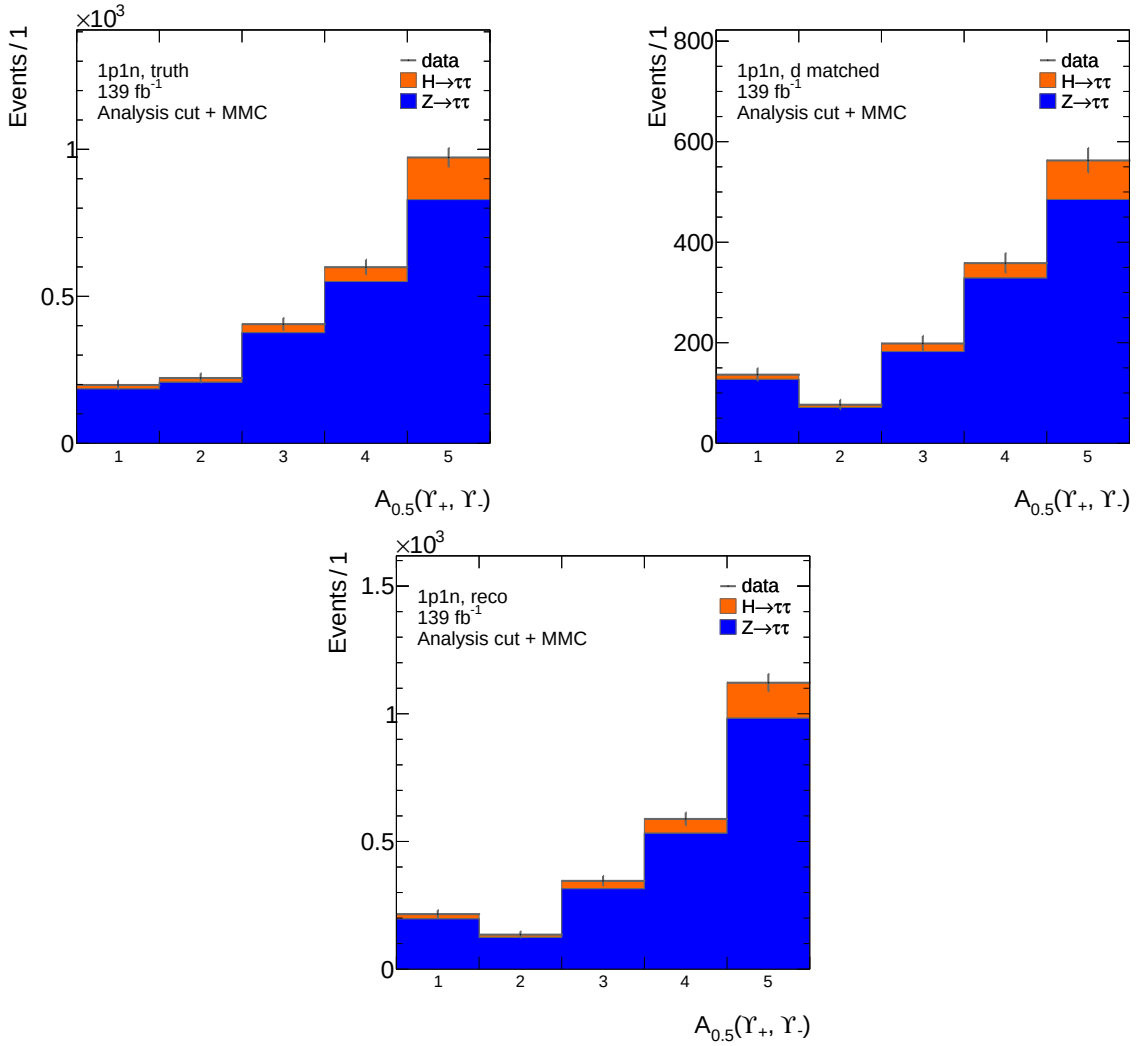

Figure 5.11: $A_{0.5}(\Upsilon_+, \Upsilon_-)$ for the analysis cut + MMC for the three different cases. H and Z are stacked and the errors are the Poisson errors for the events of both particles together. LHC Run 2 data is used (simulated ATLAS $Z \to \tau\tau$ and $H \to \tau\tau$ events).

Table 5.1: Significances $\tilde{Z}_{0,\{s_i+b_i\}}$ (Eq. (2.4)) for $A_{0.5}(\Upsilon_+, \Upsilon_-)$ for different cuts and cases. As a comparison the signal to background ratios are assumed to be constant for each bin of $A_{0.5}(\Upsilon_+, \Upsilon_-)$ and $\tilde{Z}_{0,s+b}$ (Eq. (2.3)) is calculated.

	truth		d matched		reco	
	$\tilde{Z}_{0,s+b}$	$\tilde{Z}_{0,\{s_i+b_i\}}$	$\tilde{Z}_{0,s+b}$	$\tilde{Z}_{0,\{s_i+b_i\}}$	$\tilde{Z}_{0,s+b}$	$\tilde{Z}_{0,\{s_i+b_i\}}$
Q and d cut	5.272	5.611	4.199	4.352	5.815	5.919
Analysis cut	2.584	2.702	1.967	2.029	2.662	2.702
Analysis cut + MMC	5.278	5.640	3.927	4.108	5.403	5.485

are used. $\Upsilon_\pm$ relies on the 1p1n decay mode and using wrong decay modes in the calculations weakens the observed effect.

The reco case is the most interesting because it is closest to the real data obtained in the experiment. The gains in sensitivity are 0.104 for the Q and d cut, 0.04 for the analysis cut and 0.082 for the analysis cut + MMC. These values are quite small but there is some gain in sensitivity and considering the large background and only small signal there is no huge gain in sensitivity to be expected. However, there are ideas to further improve this that will be discussed below in this chapter and briefly in Chapter 7.

The projection function $A_b(\Upsilon_+, \Upsilon_-)$ can be optimised in the choice of b. An idea to improve the projection would be to use four parameters to individually optimise the borders of the areas shown in Fig. 5.5. But because the choice of $b = 0.5$ is also logically reasonable for all borders as discussed above, this will probably have only a small effect.

Because $A_{0.5}(\Upsilon_+, \Upsilon_-) = 5$ has the most differences, another idea would be to split this bin up into two bins. Selecting the left and bottom area with the number 5 into one bin, because they look somewhat similar in the H histograms, and the other two areas into another bin has no effect on the gained sensitivities.

5.4 Multiple mass bins

As mentioned before many analyses use the particle mass to find or identify particles. If the discussed polarisation observable is used in a SM H analysis, it would be used together with the mass to increase sensitivity. In such an analysis multiple mass bins are used. To get an idea how $\Upsilon_\pm$ could increase the sensitivity in an analysis that uses multiple mass bins, $A_{0.5}(\Upsilon_+, \Upsilon_-)$ is extended to also split the events by their mass. This leads to the new projection function

$$A_{0.5,n}^{[m_l,m_u]}(\Upsilon_+, \Upsilon_-, m_{\tau\tau}^{\text{MMC}}) = \begin{cases} 0 \cdot 5 + A_{0.5}(\Upsilon_+, \Upsilon_-), & \text{if } m_l \leq m_{\tau\tau}^{\text{MMC}} < m_l + \mu \\ 1 \cdot 5 + A_{0.5}(\Upsilon_+, \Upsilon_-), & \text{if } m_l + \mu \leq m_{\tau\tau}^{\text{MMC}} < m_l + 2 \cdot \mu \\ \dots & \\ (n-1) \cdot 5 + A_{0.5}(\Upsilon_+, \Upsilon_-), & \text{if } m_u - \mu \leq m_{\tau\tau}^{\text{MMC}} < m_u \end{cases}$$

with $\mu = (m_u - m_l)/n$ that splits $A_{0.5}(\Upsilon_+, \Upsilon_-)$ into n equidistant mass bins between m_l and m_u. This projection automatically applies a $m_{\tau\tau}^{\text{MMC}}$ cut and thus, only the analysis cut + MMC is analysed. The bounds of the $m_{\tau\tau}^{\text{MMC}}$ cut are also used in the new projection function as $m_l = 110\,\text{GeV}$ and $m_u = 140\,\text{GeV}$. Because this functions creates $n \cdot 5$ bins $n = 3$ is chosen to have enough statistics in

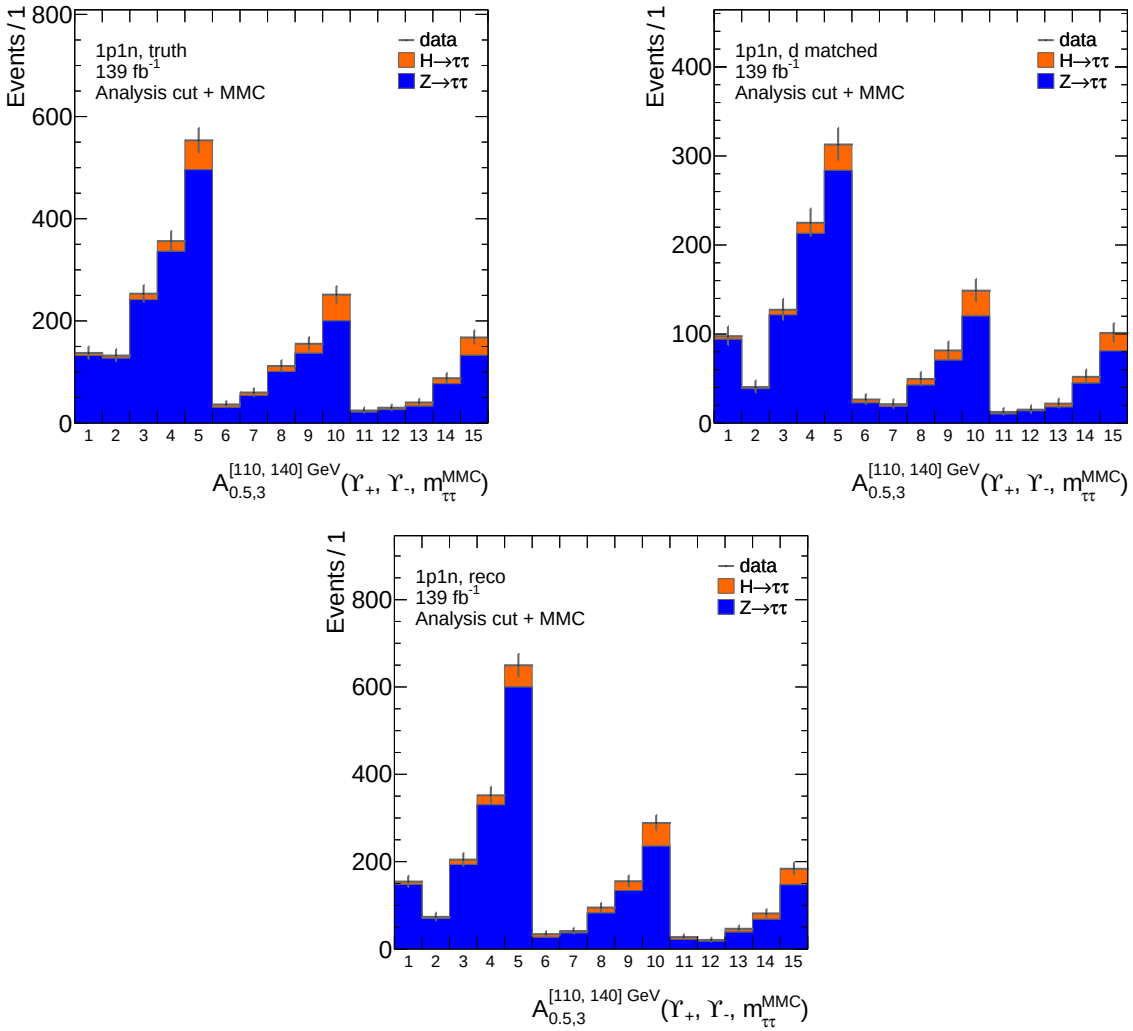

Figure 5.12: $A_{0.5,3}^{[110,140]\text{GeV}}(\Upsilon_+, \Upsilon_-, m_{\tau\tau}^{\text{MMC}})$ for different cases with the analysis cut + MMC. Bins 1-5 show $A_{0.5}(\Upsilon_+, \Upsilon_-)$ for 110 GeV $\leq m_{\tau\tau}^{\text{MMC}} <$ 120 GeV, bins 6-10 for 120 GeV $\leq m_{\tau\tau}^{\text{MMC}} <$ 130 GeV and bins 11-15 for 130 GeV $\leq m_{\tau\tau}^{\text{MMC}} <$ 140 GeV. LHC Run 2 data is used (simulated ATLAS $Z \to \tau\tau$ and $H \to \tau\tau$ events).

all bins. The result is shown in Fig. 5.12.

To see how the sensitivity is improved, the significances are calculated with Eq. (2.4). These values are compared to significances if only the mass is used to split the data into different bins using

$$\text{split}_n^{[m_l, m_u]}(m_{\tau\tau}^{\text{MMC}}) = \begin{cases} 0, & \text{if } m_l \leq m_{\tau\tau}^{\text{MMC}} < m_l + \mu \\ 1, & \text{if } m_l + \mu \leq m_{\tau\tau}^{\text{MMC}} < m_l + 2 \cdot \mu \\ \dots & \\ (n-1), & \text{if } m_u - \mu \leq m_{\tau\tau}^{\text{MMC}} < m_u \end{cases}$$

where m_l and m_u are chosen like in $A_{0.5,n}^{[m_l,m_u]}(\Upsilon_+, \Upsilon_-, m_{\tau\tau}^{\text{MMC}})$. As a comparison $n = 3$ is chosen because $A_{0.5}(\Upsilon_+, \Upsilon_-)$ is also split into three mass bins. Another comparison is done using $n = 5$ in $\text{split}_n^{[m_l,m_u]}(m_{\tau\tau}^{\text{MMC}})$ because $A_{0.5}(\Upsilon_+, \Upsilon_-)$ splits the data into five bins.

All significances are shown in Table 5.2. In all cases the sensitivity is improved compared to just using the mass. The biggest improvement is again in the truth case. The d matched sensitivities are again lower because of less events but the improvements are higher than in the reco case. The reason for this is again the additional truth decay mode information that is used. The improvements are also higher than in Table 5.1 where the mass is not used. But when using the mass the calculated significances are also higher which may cause the differences to increase. Also only using the mass delivers higher significances than only using $A_{0.5}(\Upsilon_+, \Upsilon_-)$. Thus, as expected, the mass is the more sensitive observable, at least when using $A_{0.5}(\Upsilon_+, \Upsilon_-)$. However, the spin information, that is accessed through $\Upsilon_\pm$, can increase the sensitivity of an analysis that searches for H with Z as background.

Table 5.2: Significances $\tilde{Z}_{0,\{s_i+b_i\}}$ (Eq. (2.4)) for $\text{A}_{0.5,3}^{[110,140]\text{GeV}}(\Upsilon_+, \Upsilon_-, m_{\tau\tau}^{\text{MMC}})$ and $\text{split}_{3,5}^{[110,140]\text{GeV}}(m_{\tau\tau}^{\text{MMC}})$ for comparison.

	$\tilde{Z}_{0,\{s_i+b_i\}}$ (truth)	$\tilde{Z}_{0,\{s_i+b_i\}}$ (d matched)	$\tilde{Z}_{0,\{s_i+b_i\}}$ (reco)
$\text{split}_3^{[110,140]\text{GeV}}(m_{\tau\tau}^{\text{MMC}})$	5.794	4.406	6.100
$\text{split}_5^{[110,140]\text{GeV}}(m_{\tau\tau}^{\text{MMC}})$	5.841	4.423	6.139
$\text{A}_{0.5,3}^{[110,140]\text{GeV}}(\Upsilon_+, \Upsilon_-, m_{\tau\tau}^{\text{MMC}})$	6.137	4.548	6.201

CHAPTER 6

Conclusion

A possibility to access Z and H spin information in the $\tau\tau$ channel by analysing the τ decay products in the 1p1n decay has been presented. The observable that can be used to obtain this information is the charged energy asymmetry $\Upsilon_{\pm}$. The analysis uses simulated data, corresponding to Run 2 data from the LHC, where ATLAS recorded 139 fb^{-1} of data. Different cuts were applied to the data and three combinations of cuts were analysed. The first combination consists of a charge, a decay mode and for the Z a MC weight cut. The second combination adds some cuts from a SM H analysis [8]. In the last combination a cut using the invariant mass is introduced in addition to the analysis cut. For every cut three cases were analysed. One case only uses truth information, but this information has a bias because events are only available if two τ-leptons were reconstructed. In the second case reconstructed information and the truth decay mode are used, and in the last case only reconstructed information is used.

To obtain information about the initial particle (Z or H) spin the correlation between Υ_+ and Υ_- was analysed for all cases and cuts mentioned above. In the two-dimensional histograms shape differences are clearly visible. Because there are some bins with less statistics, especially when applying the analysis cut, these histograms were projected into one dimension with $A_b(\Upsilon_+, \Upsilon_-)$. This function divides the histograms into different areas to select the areas with differences for Z and H. The optimal choice of the parameter b is $b = 0.5$. Applying cuts does not really affect the shape of $A_b(\Upsilon_+, \Upsilon_-)$.

The significances were calculated with the Asimov estimate for discovery significance for $A_{0.5}(\Upsilon_+, \Upsilon_-)$ for the different cuts and cases. As a comparison the significance was calculated using the sum of all signal events as signal and the sum of all background events as background. In all cases the sensitivity is improved. Because of the bias in the truth case it is not useful to compare this case to the others. The significances in the d matched case are smaller than in the reco case because of less events. However, the sensitivity improvement is better in the d matched case because the truth decay mode information is used. Sensitivity improvements are present but rather small. This could be improved by optimising the projection from the two-dimensional histogram or using the information of the two-dimensional histogram. For the latter more events or a higher luminosity is necessary.

In a last step $A_b(\Upsilon_+, \Upsilon_-)$ was extended to also take the invariant mass into account. The events were split into three mass bins. This increased the calculated significances and the gained sensitivities.

The presented results show that the spin difference of Z and H is accessible through $\Upsilon_{\pm}$ for 1p1n decays in the $\tau\tau$ channel. The gained sensitivity is rather small. Optimising the projection or using other methods to use the observed differences could further improve the sensitivity.

CHAPTER 7

Outlook

There are multiple possibilities to build on the presented results. Because sensitivity is actually improved, a next step would be to integrate the analysed observable into a SM or BSM H analysis. The improvements are rather small but this thesis did not consider other backgrounds or other uncertainties. For example fake τ-leptons were not considered. This thesis showed that it is possible to use $\mathcal{Y}_{\pm}$ so the usage of this observable should be optimised in a full analysis with all backgrounds taken into account. With more events or a higher luminosity and thus, more statistics, it may be possible to use the two-dimensional information. In this case a neural network could be used in the analysis.

The analysed τ decay mode has the highest branching ratio but there are still other decay modes that could provide information on the spin of the initial particle. Other decay modes could be analysed to see if there are possibilities to access the Z and H spin. The 1p0n decay mode also has some correlation between the energy of the charged pion and the handedness of the τ [24]. This could further improve the gained sensitivity using polarisation observables.

APPENDIX A

Kinematic variables

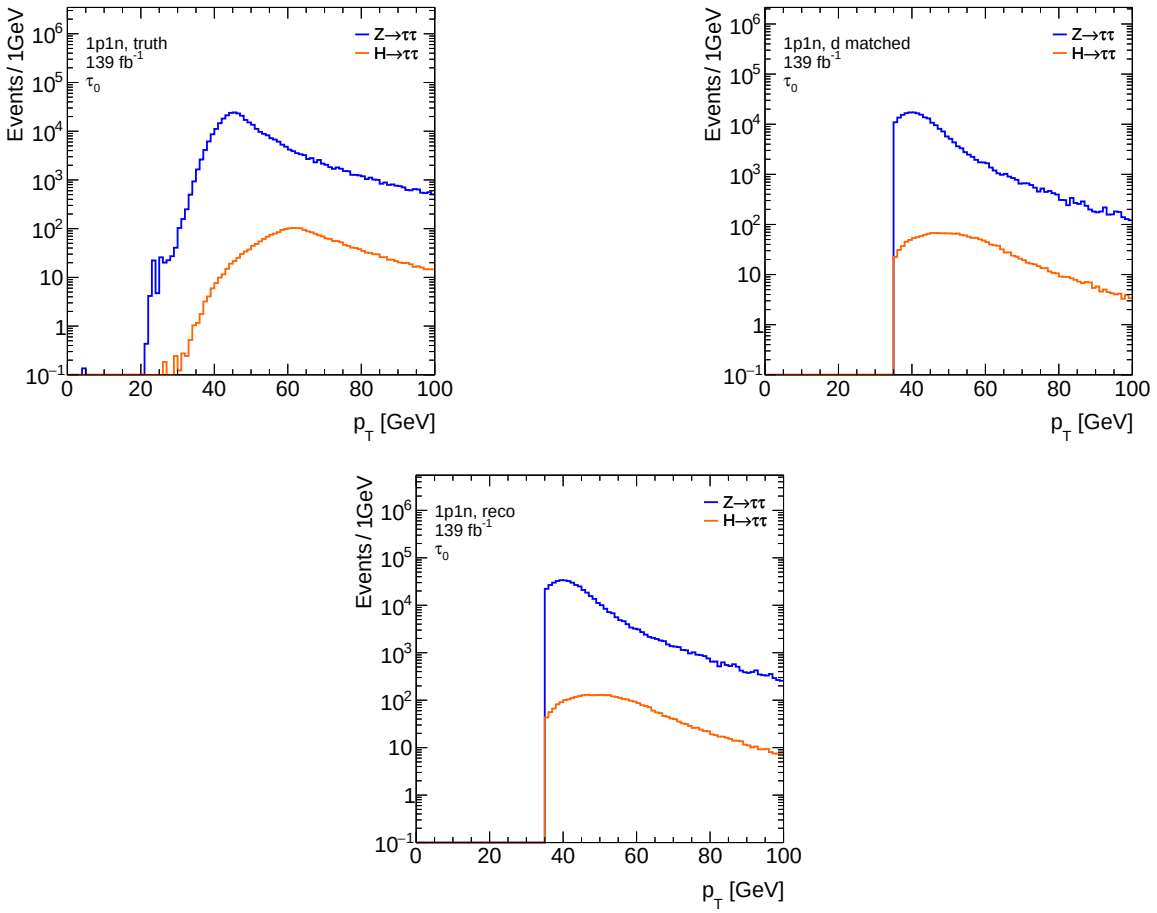

Figure A.1: Expected number of events for different leading τ (τ_0) p_{T} using LHC Run 2 data (simulated ATLAS $Z \rightarrow \tau\tau$ and $H \rightarrow \tau\tau$ events). A Q and a decay mode cut (and a MC weight cut for Z events) are applied (Chapter 4).

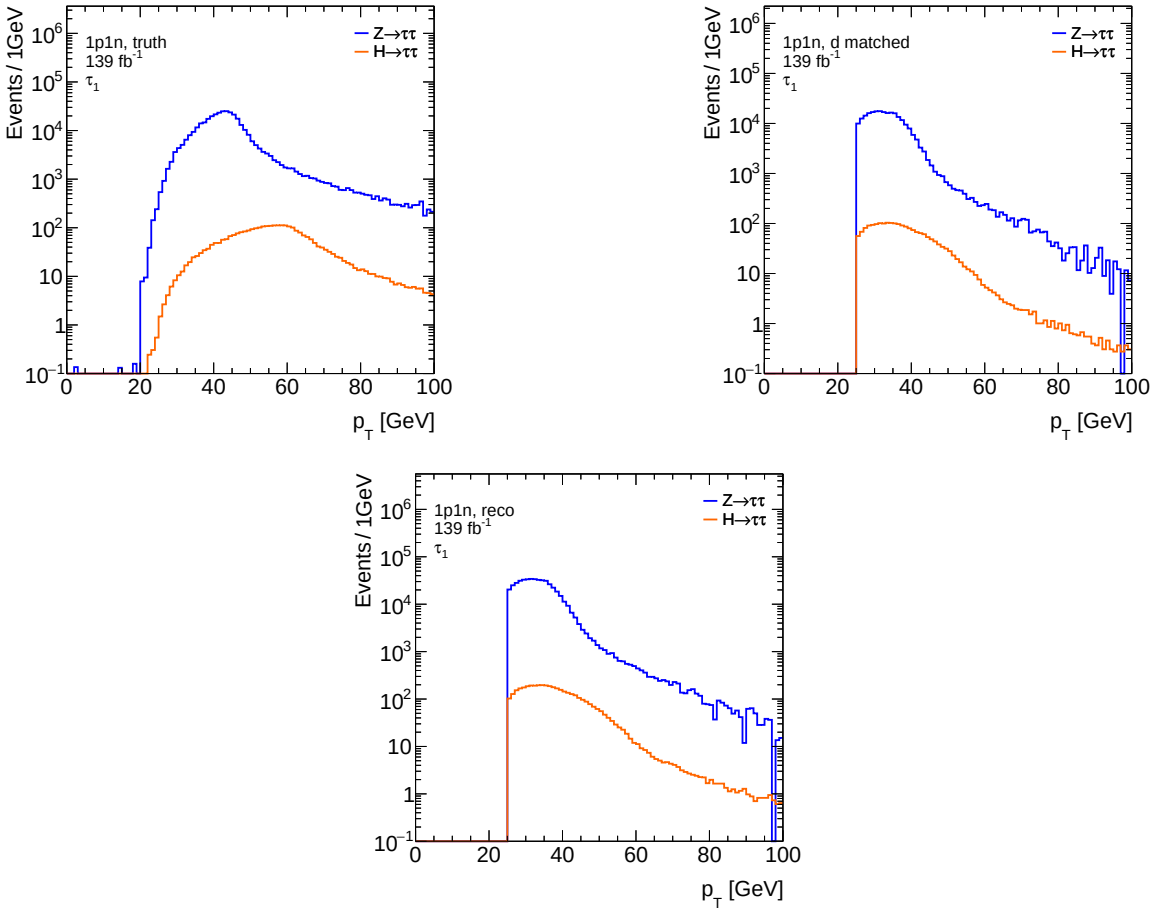

Figure A.2: Expected number of events for different sub-leading τ (τ_l) p_{T} using LHC Run 2 data (simulated ATLAS $Z \rightarrow \tau\tau$ and $H \rightarrow \tau\tau$ events). A Q and a decay mode cut (and a MC weight cut for Z events) are applied (Chapter 4).

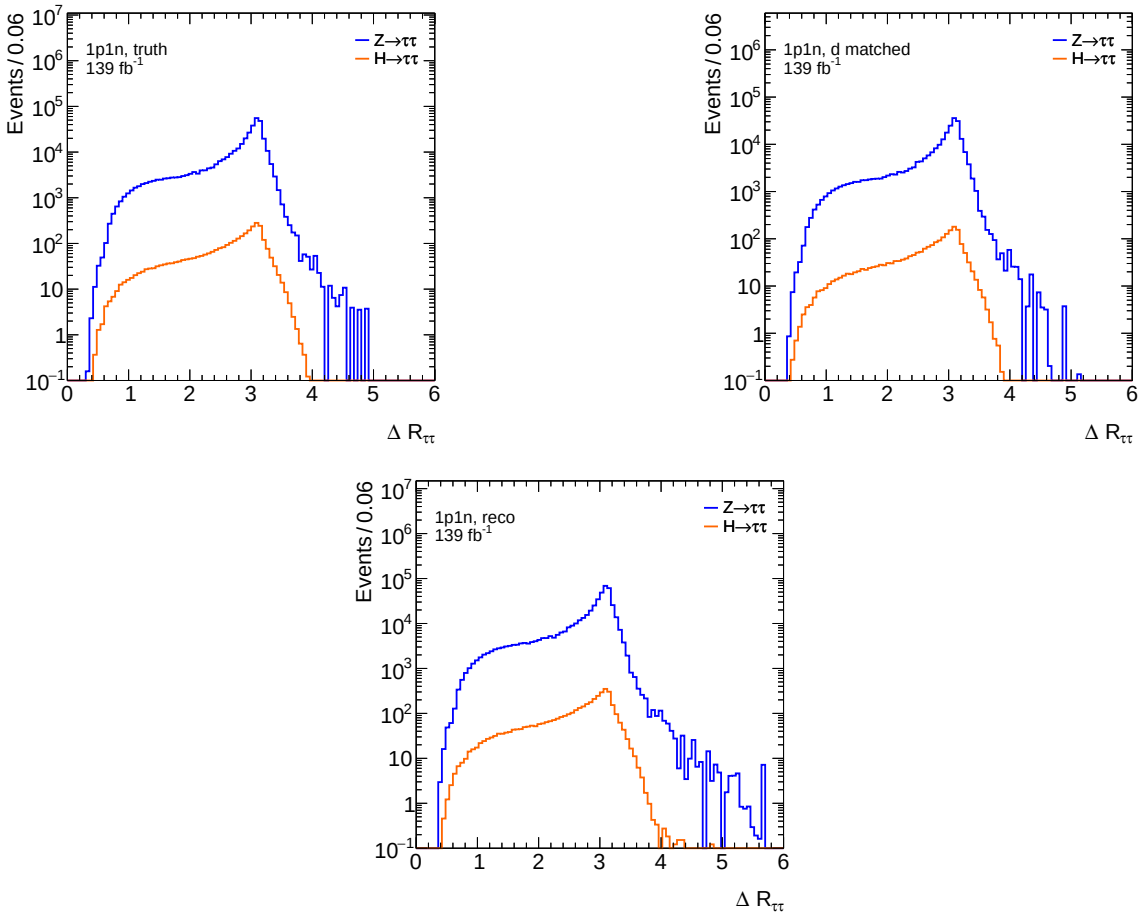

Figure A.3: Expected number of events for different $\Delta R_{\tau\tau}$ using LHC Run 2 data (simulated ATLAS $Z \rightarrow \tau\tau$ and $H \rightarrow \tau\tau$ events). A Q and a decay mode cut (and a MC weight cut for Z events) are applied (Chapter 4).

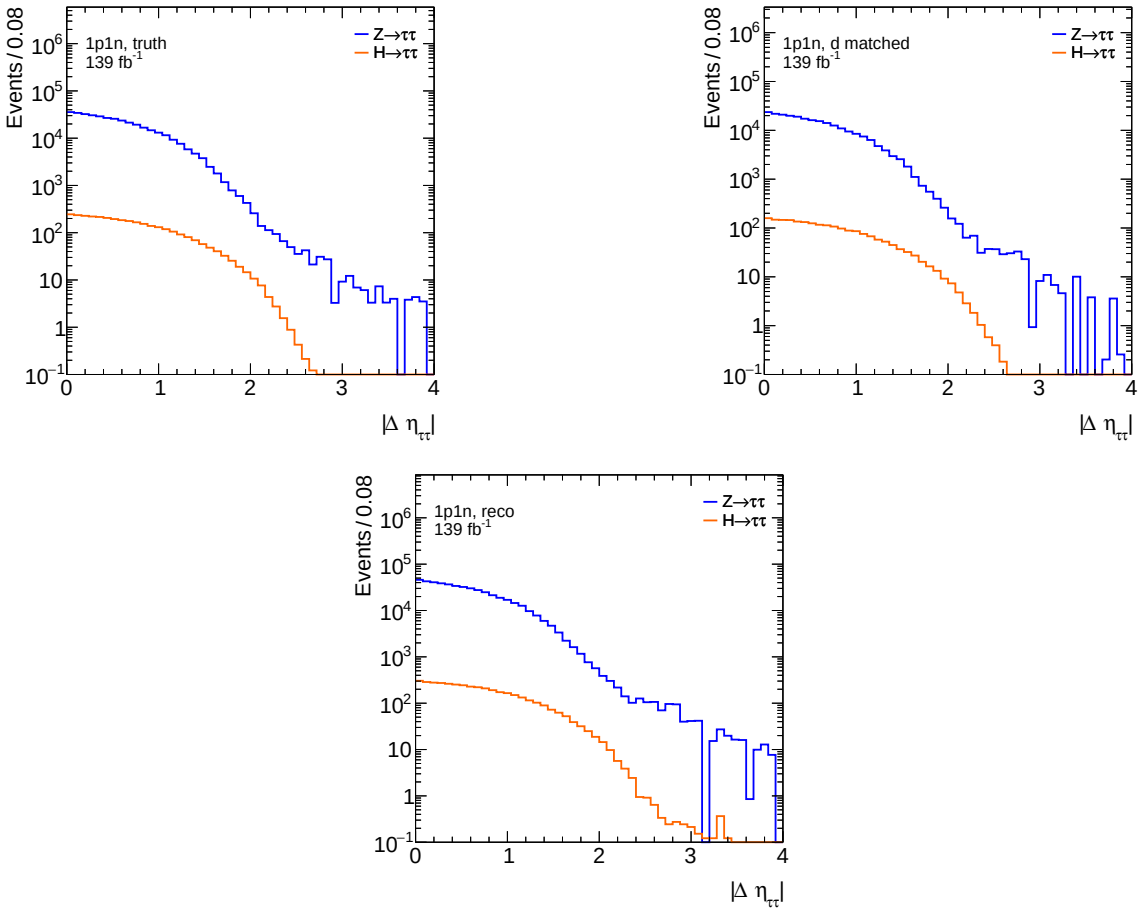

Figure A.4: Expected number of events for different $|\Delta\eta_{\tau\tau}|$ using LHC Run 2 data (simulated ATLAS $Z \to \tau\tau$ and $H \to \tau\tau$ events). A Q and a decay mode cut (and a MC weight cut for Z events) are applied (Chapter 4).

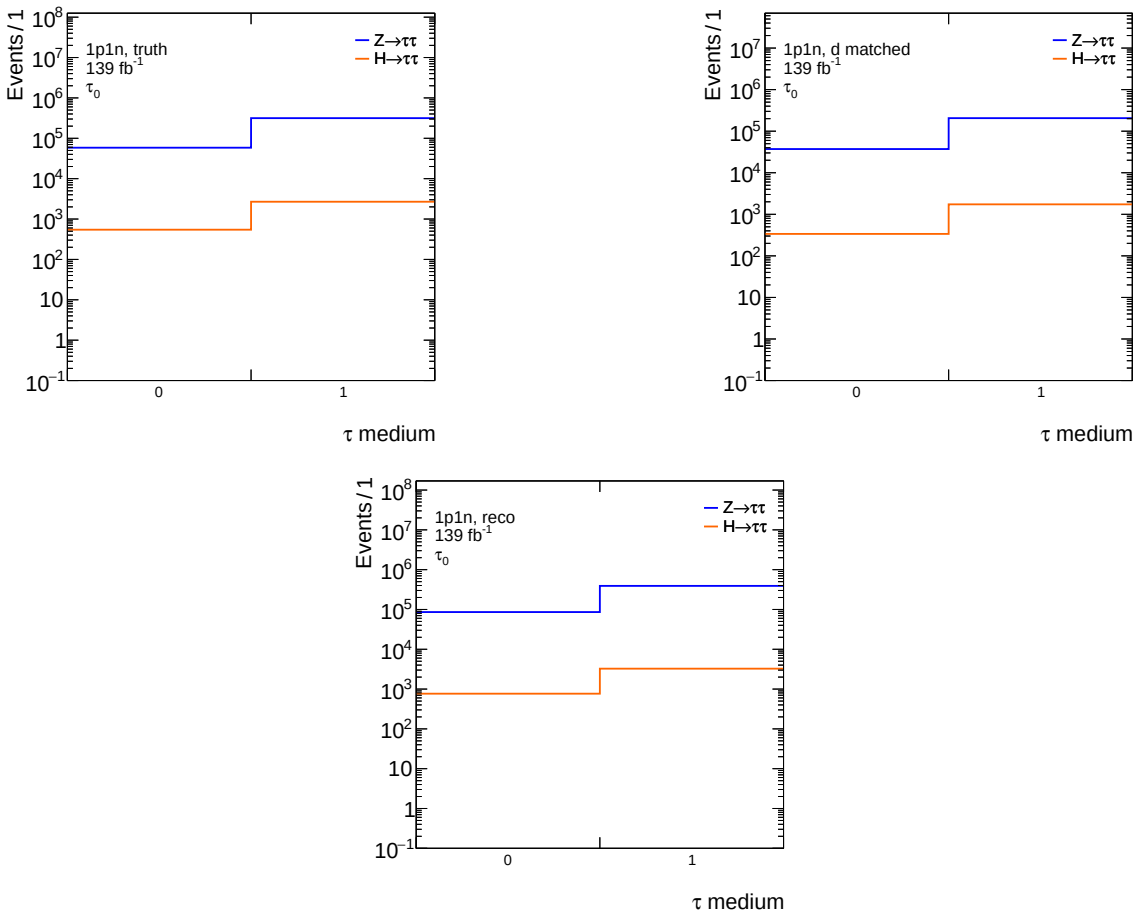

Figure A.5: Expected number of events when the leading τ (τ_0) is identified as medium (1) or not (0) using LHC Run 2 data (simulated ATLAS $Z \rightarrow \tau\tau$ and $H \rightarrow \tau\tau$ events). A Q and a decay mode cut (and a MC weight cut for Z events) are applied (Chapter 4).

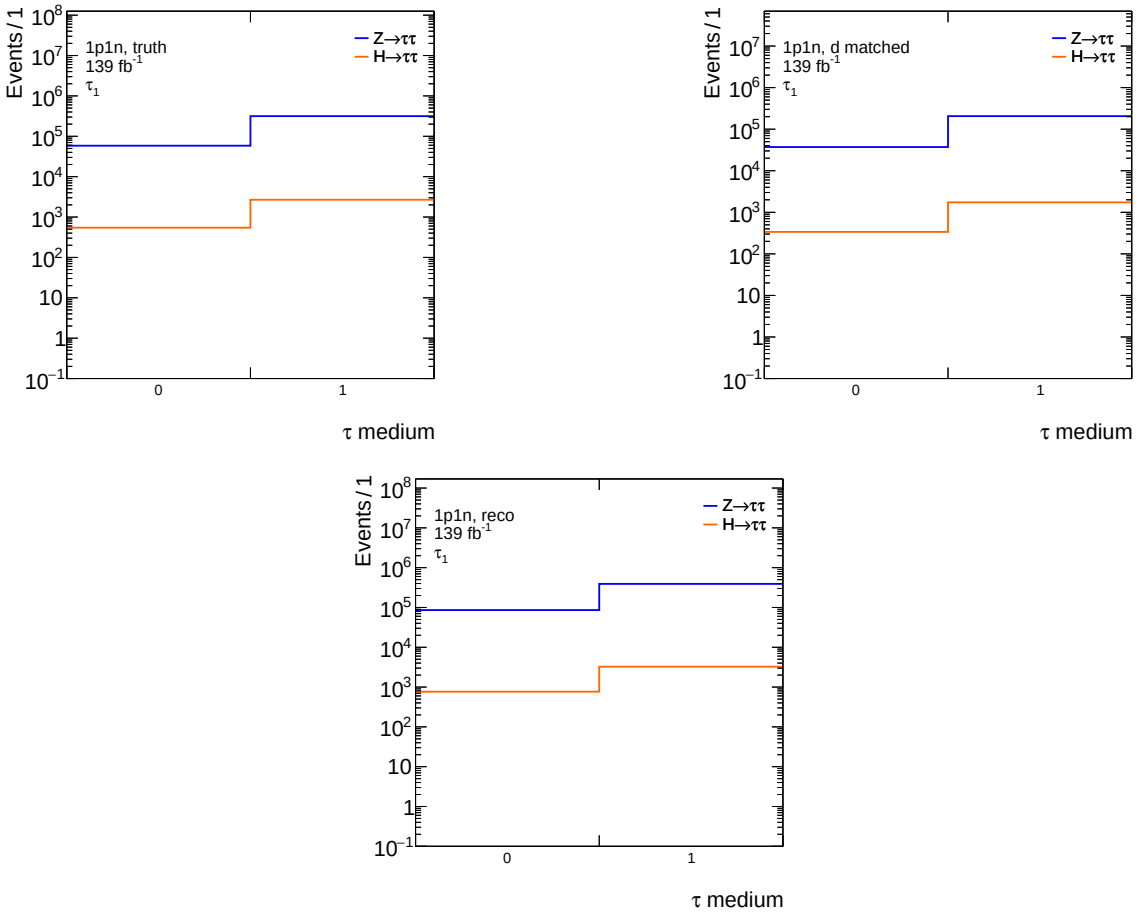

Figure A.6: Expected number of events when the sub-leading τ (τ_l) is identified as medium (1) or not (0) using LHC Run 2 data (simulated ATLAS $Z \rightarrow \tau\tau$ and $H \rightarrow \tau\tau$ events). A Q and a decay mode cut (and a MC weight cut for Z events) are applied (Chapter 4).

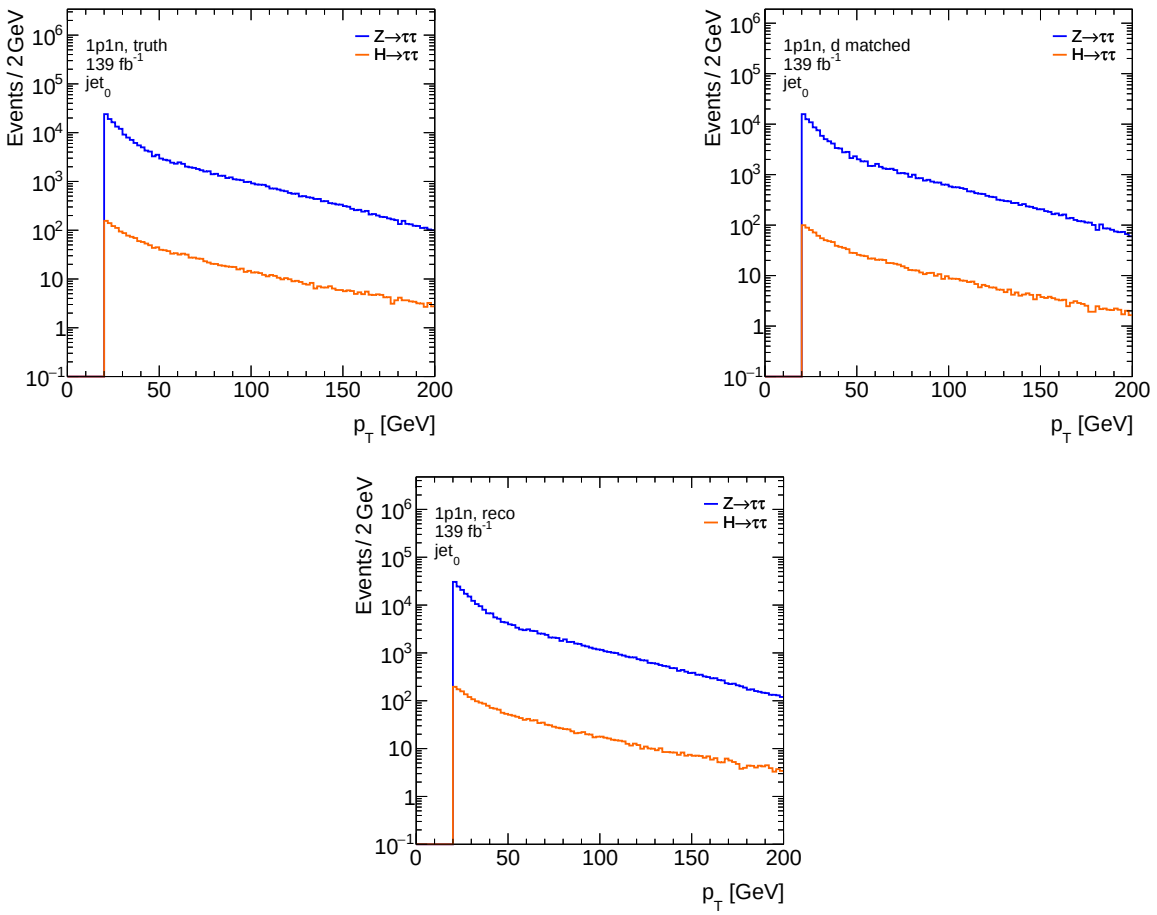

Figure A.7: Expected number of events for different leading jet (jet_0) p_{T} using LHC Run 2 data (simulated ATLAS $Z \rightarrow \tau\tau$ and $H \rightarrow \tau\tau$ events). A Q and a decay mode cut (and a MC weight cut for Z events) are applied (Chapter 4).

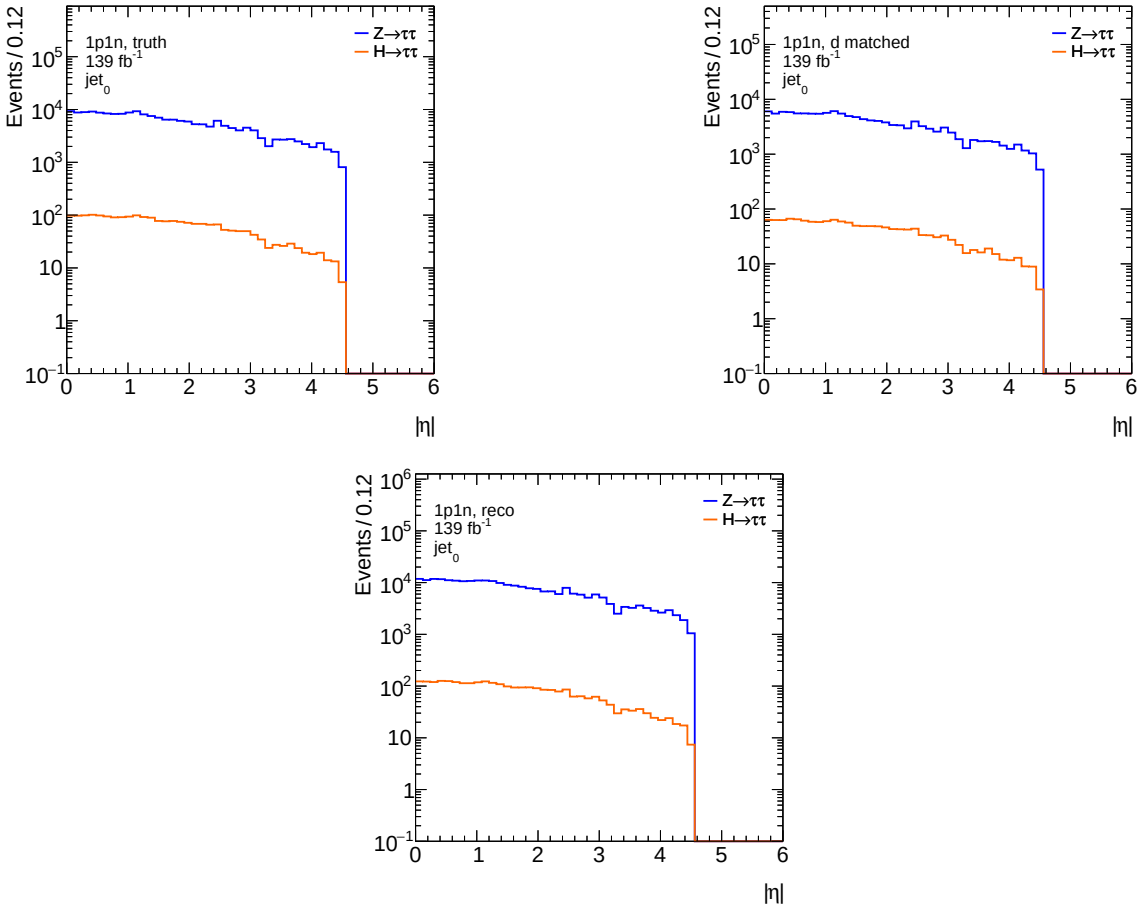

Figure A.8: Expected number of events for different leading jet (jet_0) $|\eta|$ using LHC Run 2 data (simulated ATLAS $Z \to \tau\tau$ and $H \to \tau\tau$ events). A Q and a decay mode cut (and a MC weight cut for Z events) are applied (Chapter 4).

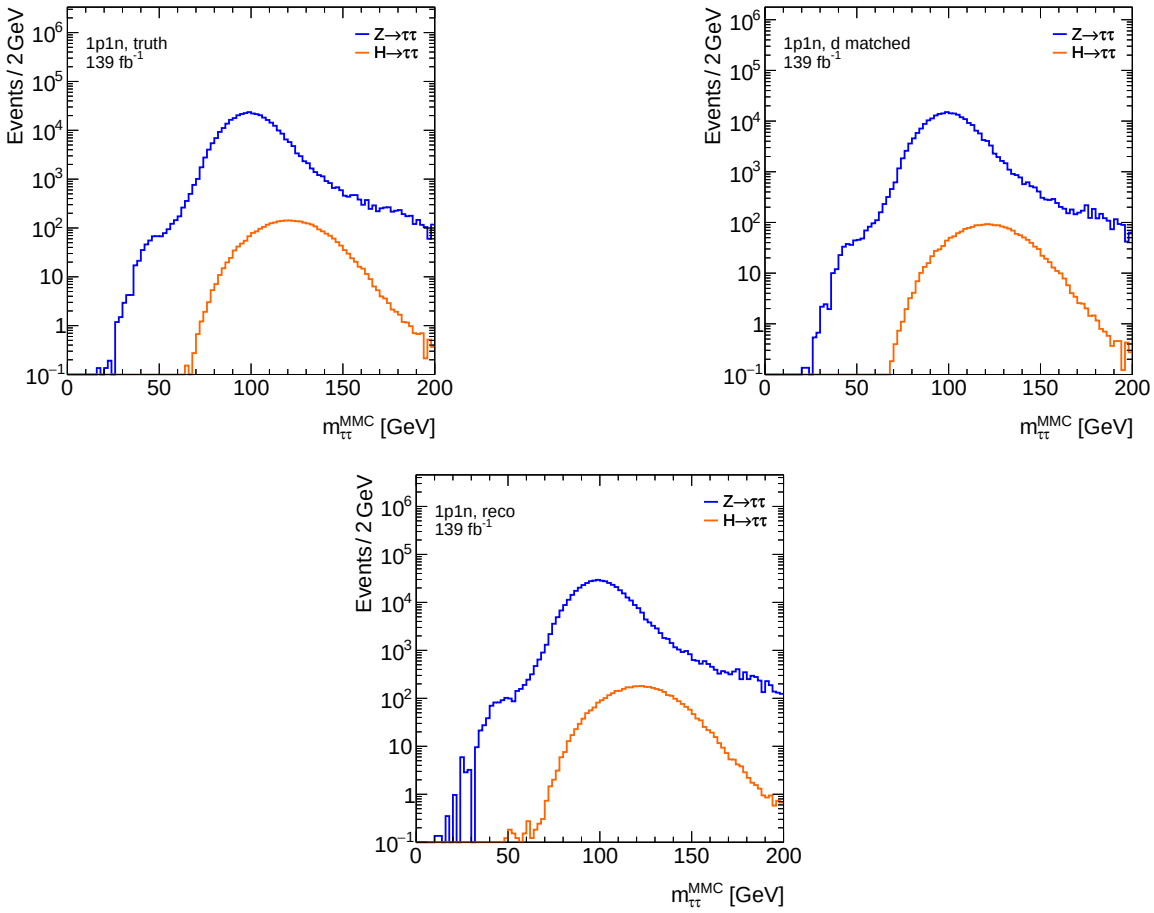

Figure A.9: Expected number of events for different invariant masses using the Missing Mass Calculator and Run 2 LHC data. A Q and a decay mode cut (and a MC weight cut for Z events) are applied (Chapter 4).

APPENDIX B

Normalised kinematic variables

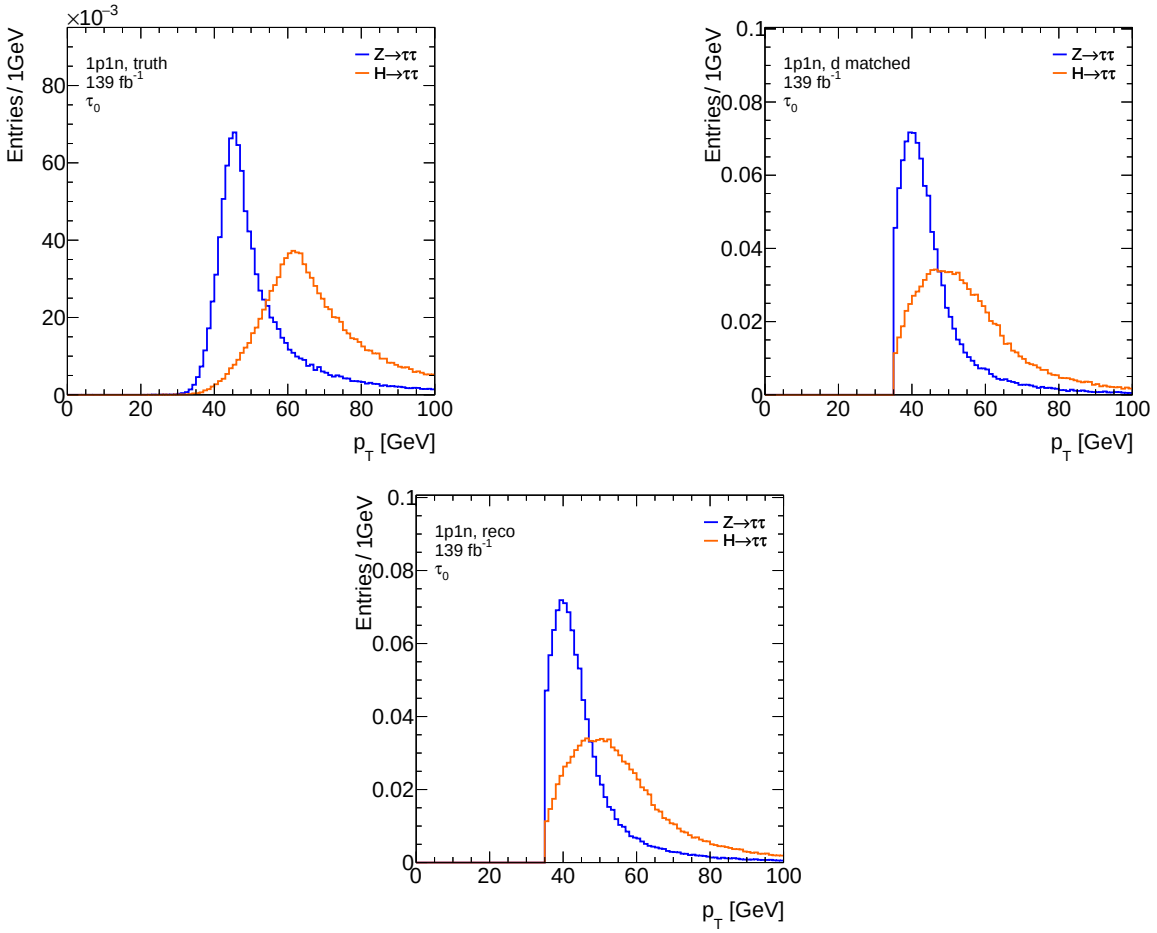

Figure B.1: Normalised leading τ (τ_0) p_{T} distribution using LHC Run 2 data (simulated ATLAS $Z \to \tau\tau$ and $H \to \tau\tau$ events). A Q and a decay mode cut (and a MC weight cut for Z events) are applied (Chapter 4).

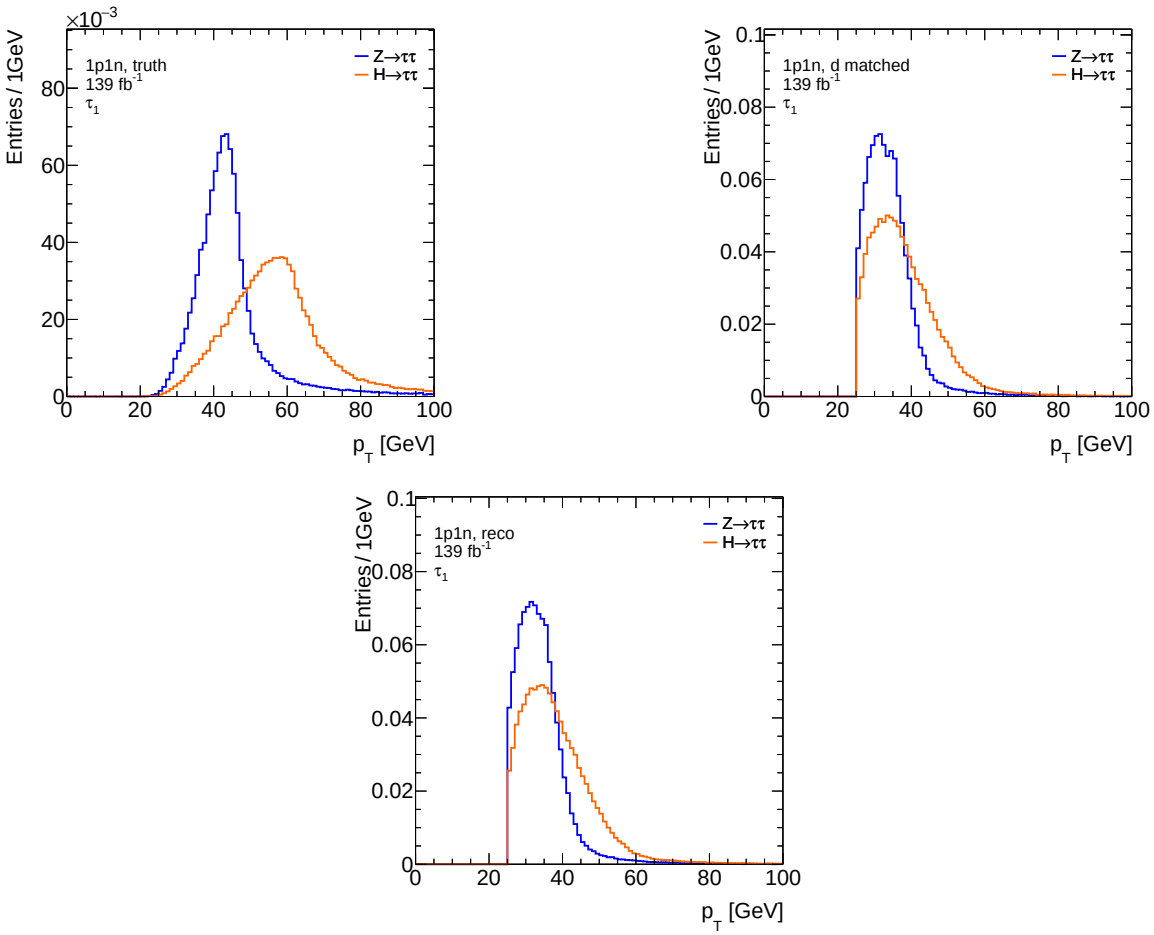

Figure B.2: Normalised sub-leading τ (τ_l) p_{T} distribution using LHC Run 2 data (simulated ATLAS $Z \rightarrow \tau\tau$ and $H \rightarrow \tau\tau$ events). A Q and a decay mode cut (and a MC weight cut for Z events) are applied (Chapter 4).

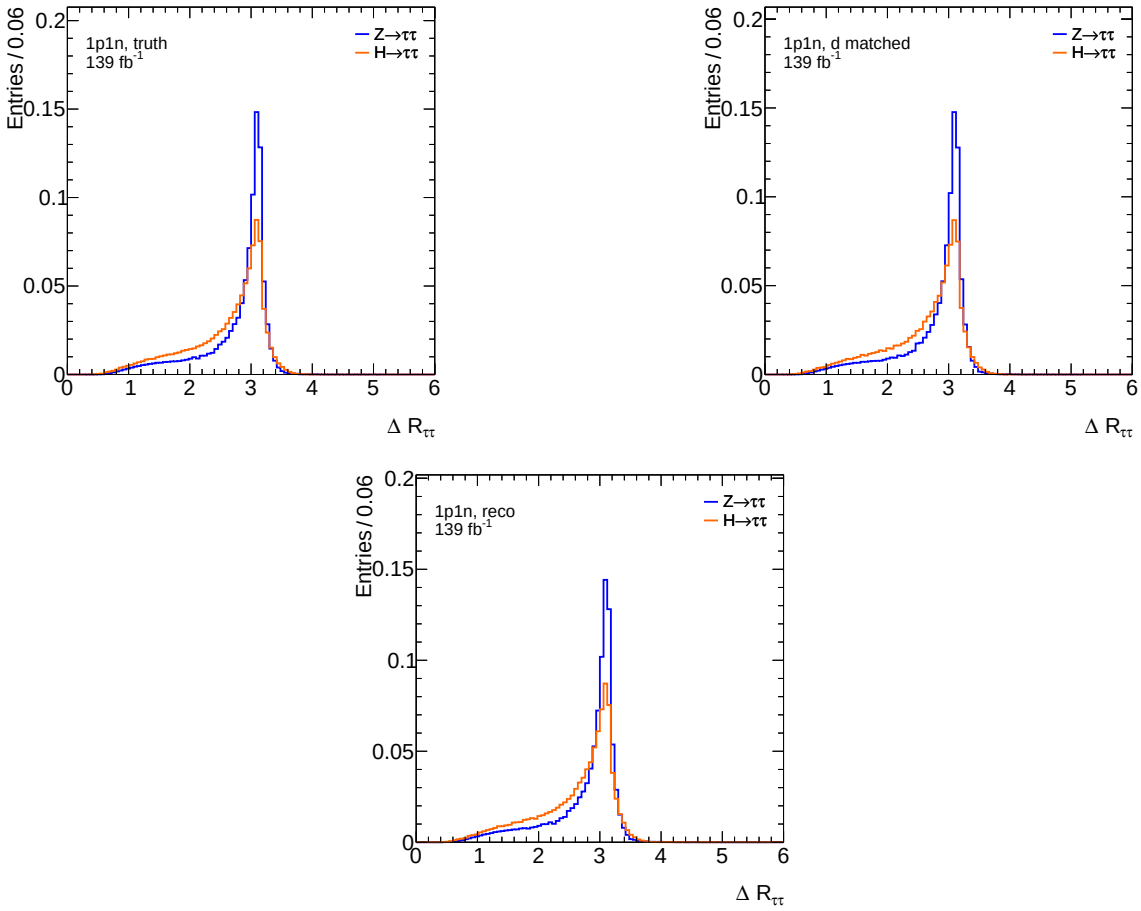

Figure B.3: Normalised $\Delta R_{\tau\tau}$ distribution using LHC Run 2 data (simulated ATLAS $Z \rightarrow \tau\tau$ and $H \rightarrow \tau\tau$ events). A Q and a decay mode cut (and a MC weight cut for Z events) are applied (Chapter 4).

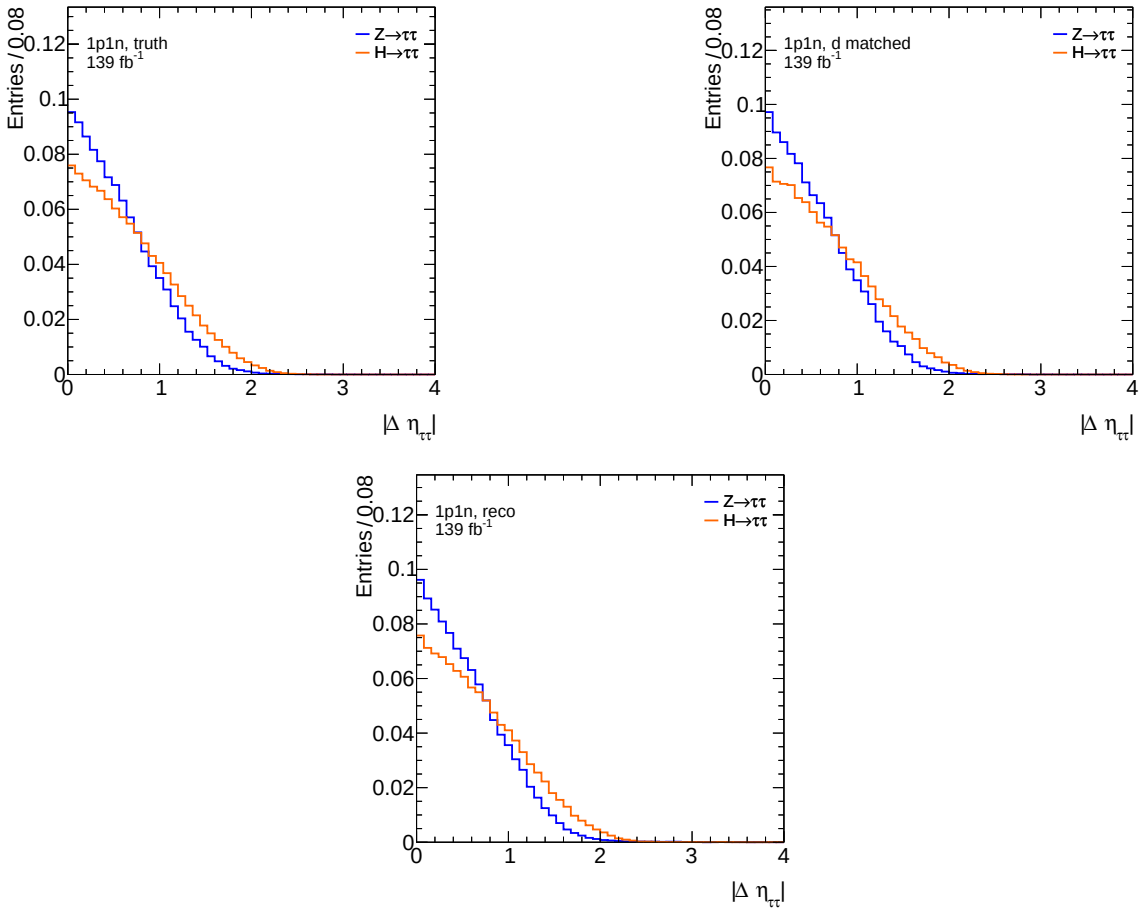

Figure B.4: Normalised $|\Delta\eta_{\tau\tau}|$ distribution using LHC Run 2 data (simulated ATLAS $Z \to \tau\tau$ and $H \to \tau\tau$ events). A Q and a decay mode cut (and a MC weight cut for Z events) are applied (Chapter 4).

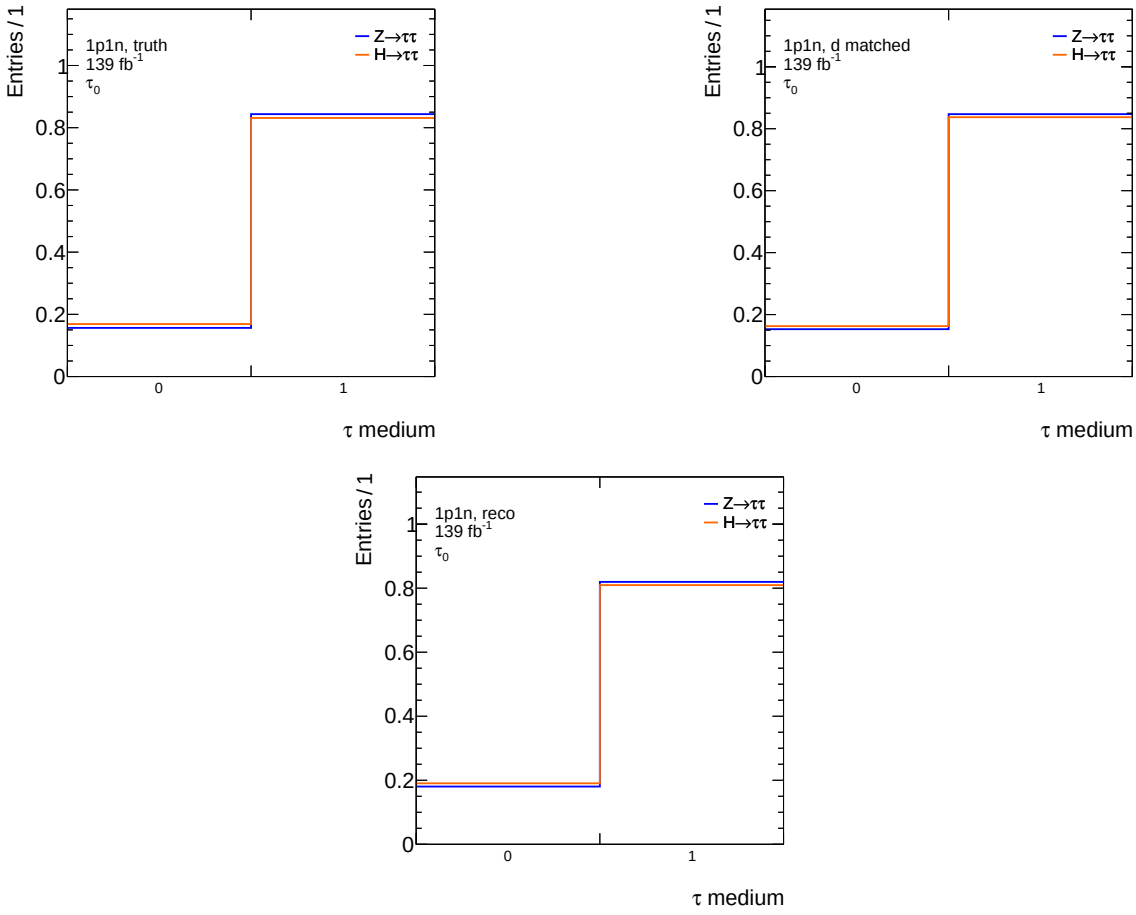

Figure B.5: Normalised distribution whether the leading τ (τ_0) is identified as medium (1) or not (0) using LHC Run 2 data (simulated ATLAS $Z \rightarrow \tau\tau$ and $H \rightarrow \tau\tau$ events). A Q and a decay mode cut (and a MC weight cut for Z events) are applied (Chapter 4).

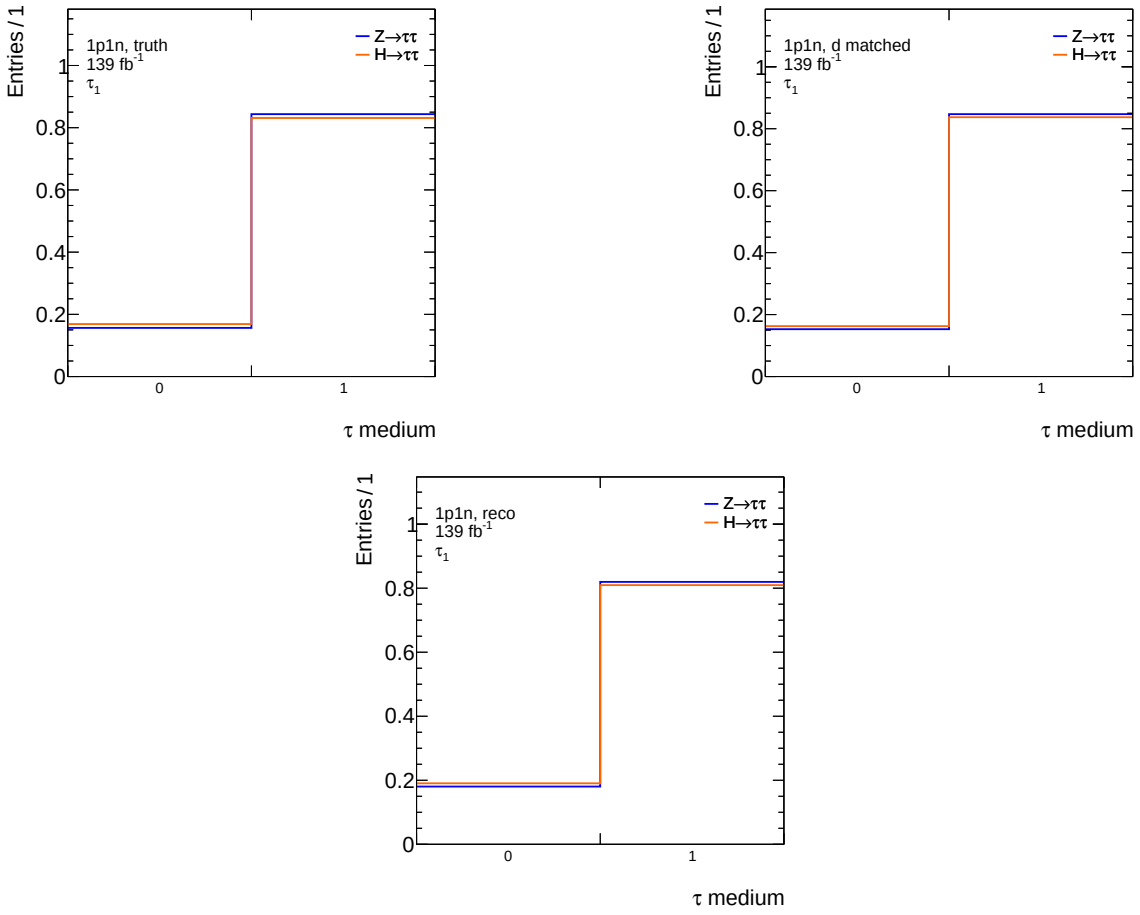

Figure B.6: Normalised distribution whether the sub-leading τ (τ_1) is identified as medium (1) or not (0) using LHC Run 2 data (simulated ATLAS $Z \rightarrow \tau\tau$ and $H \rightarrow \tau\tau$ events). A Q and a decay mode cut (and a MC weight cut for Z events) are applied (Chapter 4).

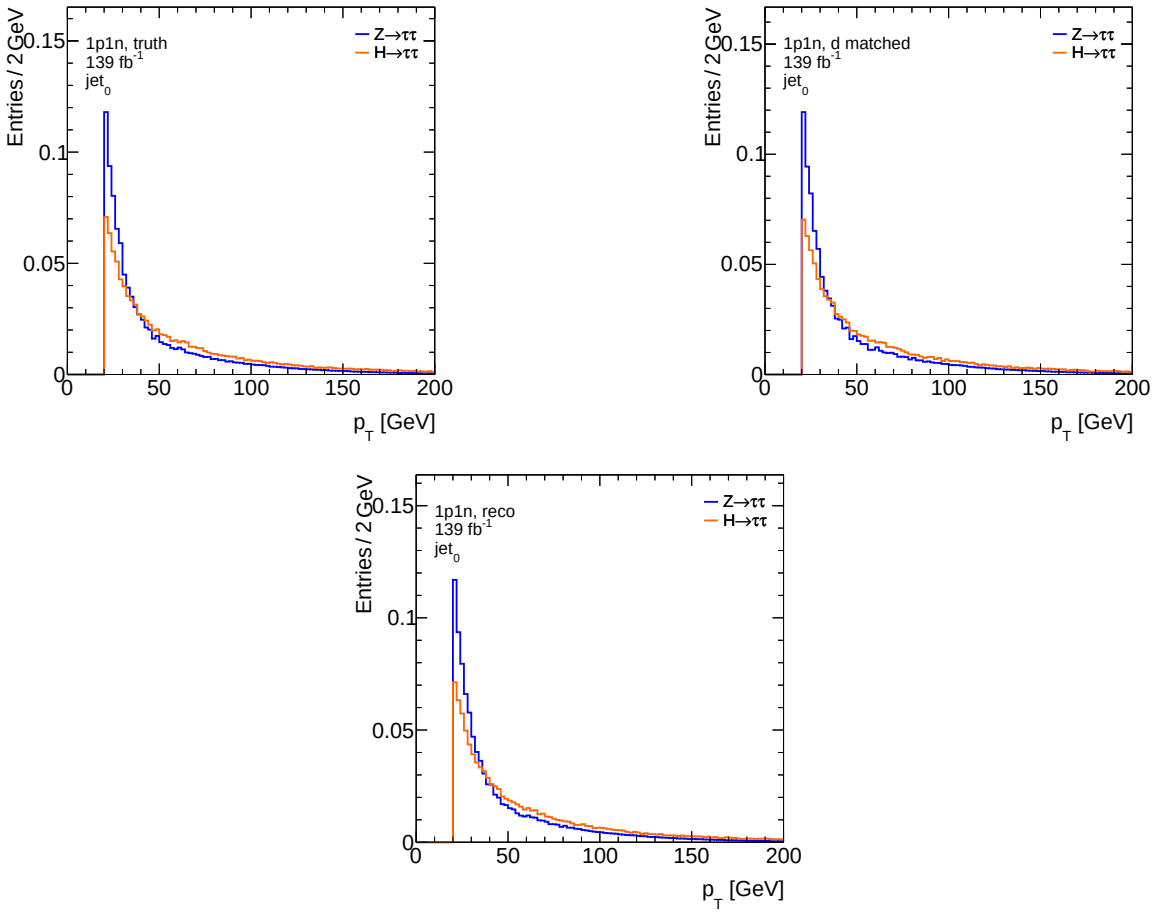

Figure B.7: Normalised leading jet (jet_0) p_{T} distribution using LHC Run 2 data (simulated ATLAS $Z \to \tau\tau$ and $H \to \tau\tau$ events). A Q and a decay mode cut (and a MC weight cut for Z events) are applied (Chapter 4).

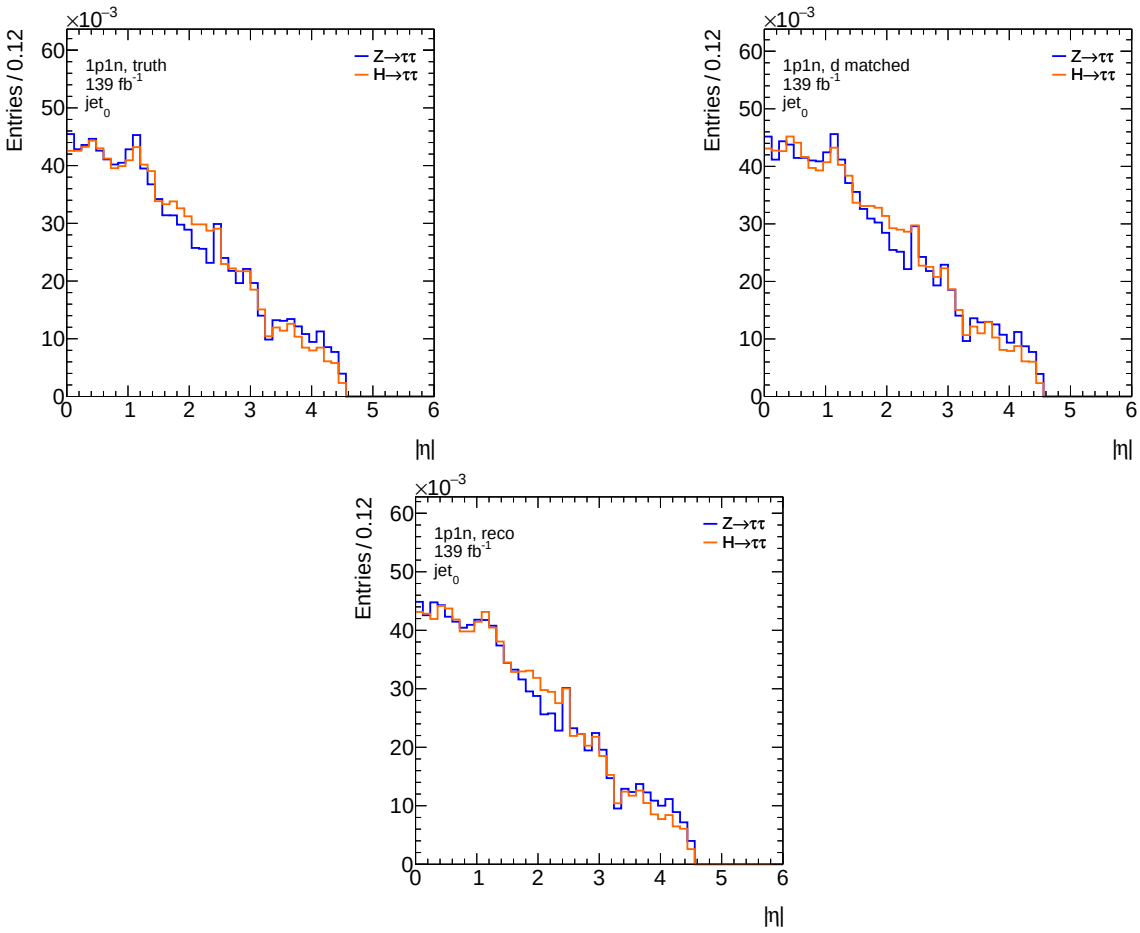

Figure B.8: Normalised leading jet (jet_0) $|\eta|$ distribution using LHC Run 2 data (simulated ATLAS $Z \to \tau\tau$ and $H \to \tau\tau$ events). A Q and a decay mode cut (and a MC weight cut for Z events) are applied (Chapter 4).

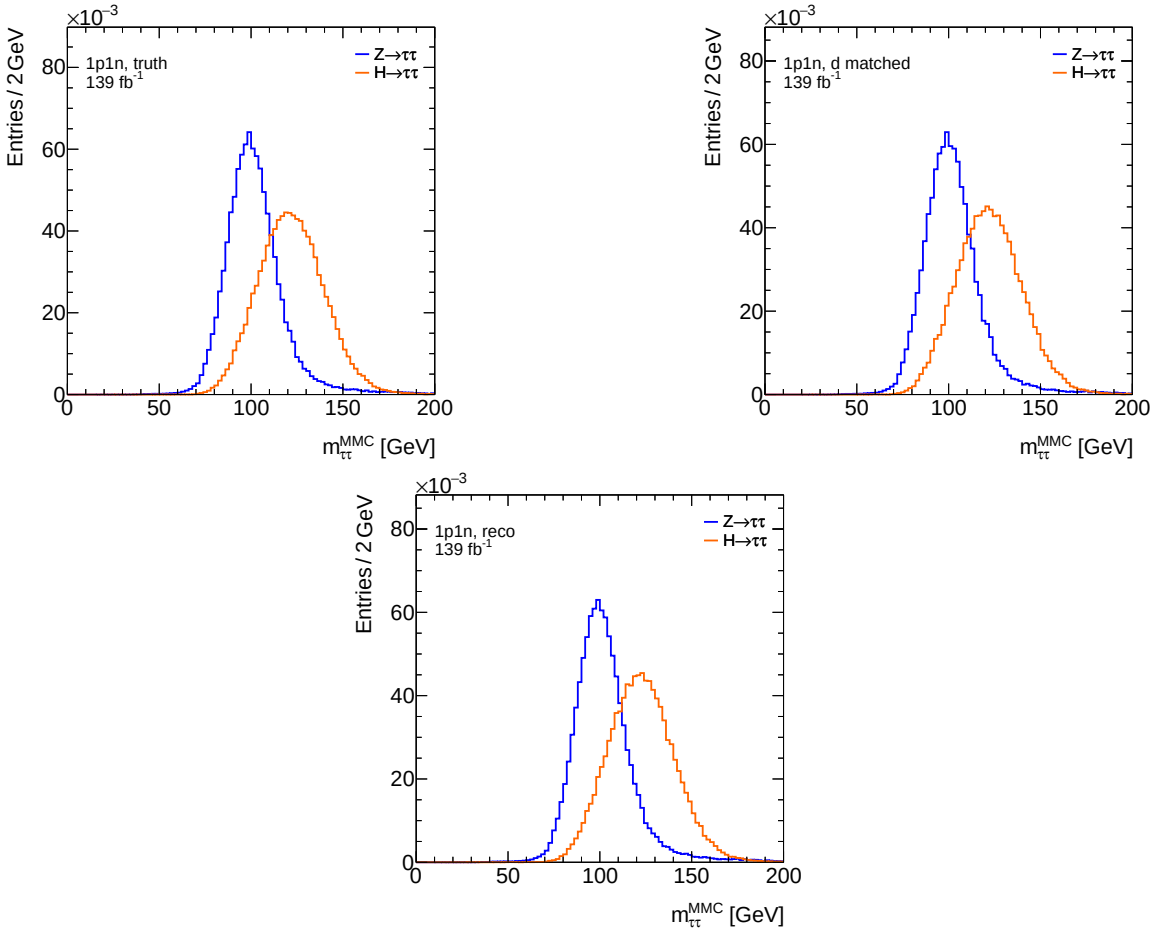

Figure B.9: Normalised invariant mass distribution using the Missing Mass Calculator and LHC Run 2 data (simulated ATLAS $Z \rightarrow \tau\tau$ and $H \rightarrow \tau\tau$ events). A Q and a decay mode cut (and a MC weight cut for Z events) are applied (Chapter 4).

APPENDIX C

Projection on logarithmic scale

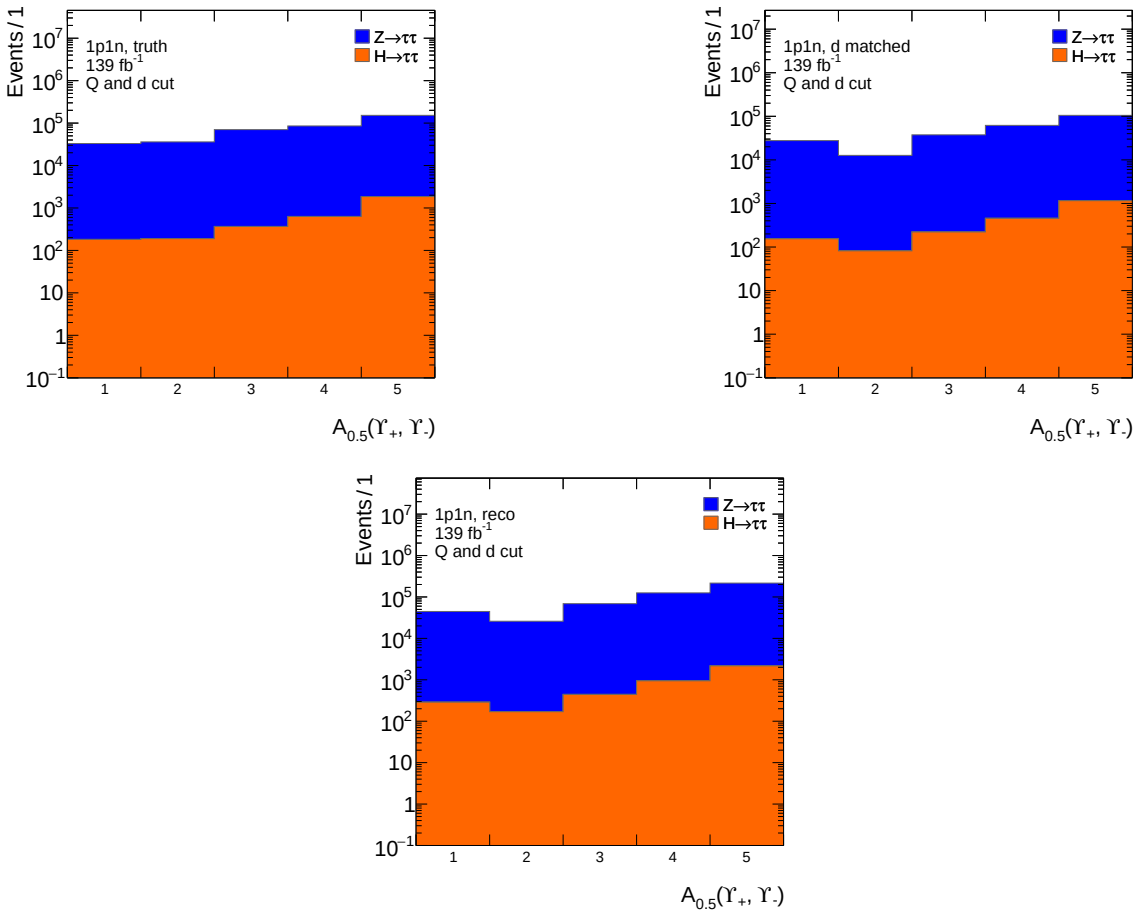

Figure C.1: $A_{0.5}(\Upsilon_+, \Upsilon_-)$ for the Q and d cut for the three different cases. H and Z are stacked. LHC Run 2 data is used (simulated ATLAS $Z \rightarrow \tau\tau$ and $H \rightarrow \tau\tau$ events).

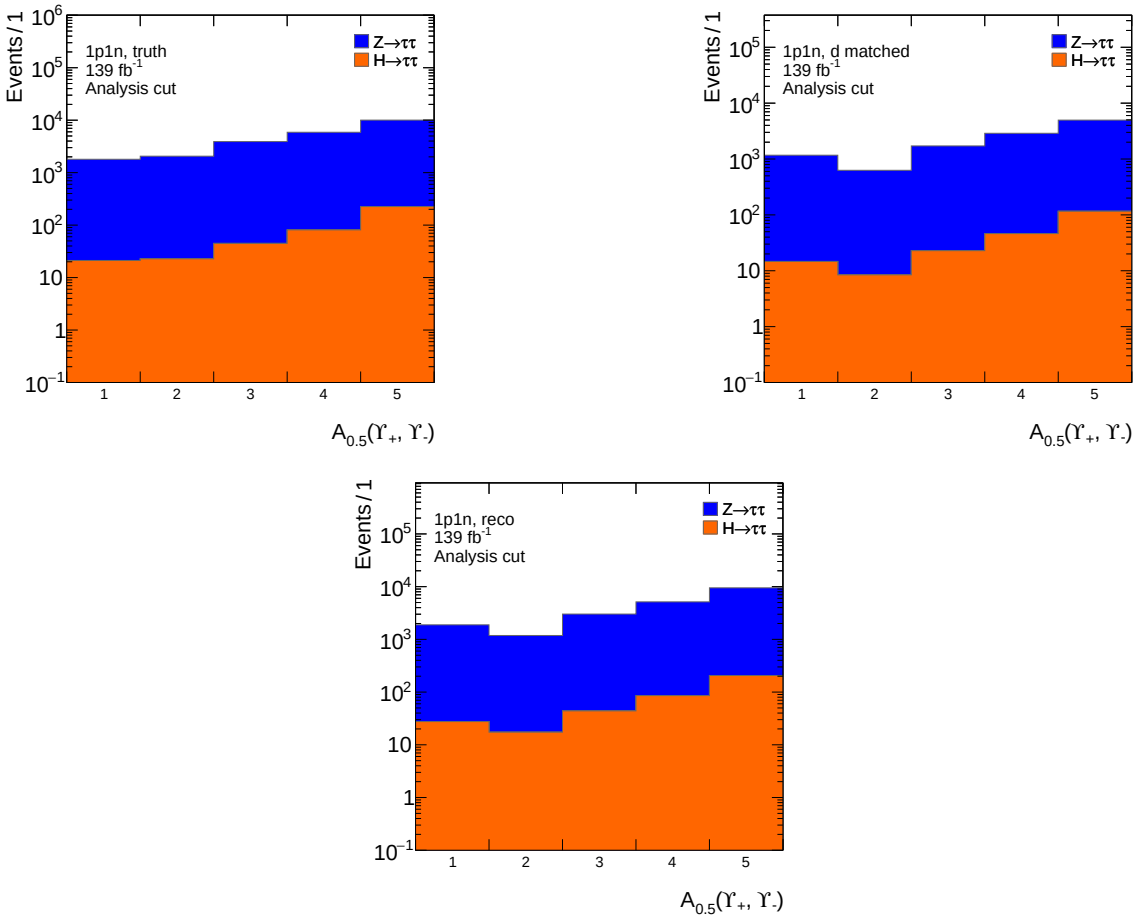

Figure C.2: $A_{0.5}(\Upsilon_+, \Upsilon_-)$ for the analysis cut for the three different cases. H and Z are stacked. LHC Run 2 data is used (simulated ATLAS $Z \to \tau\tau$ and $H \to \tau\tau$ events).

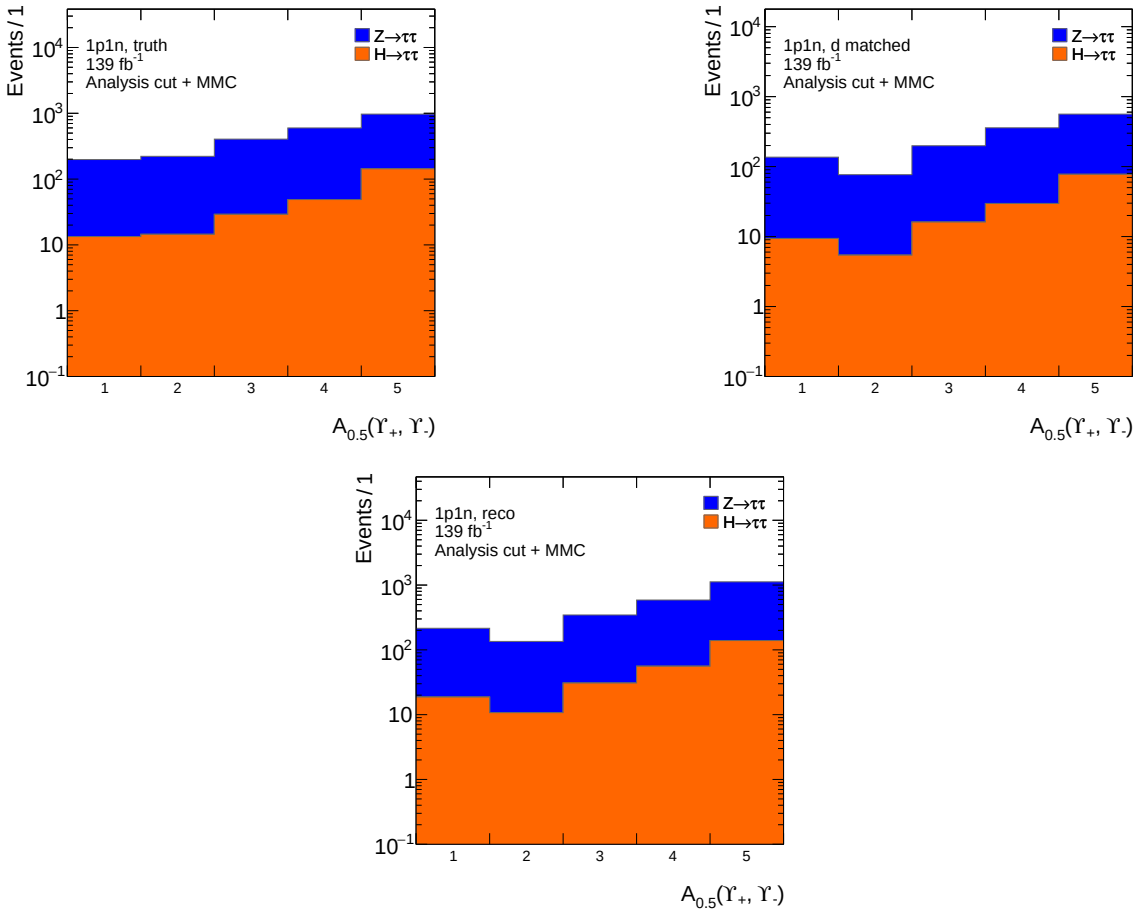

Figure C.3: $A_{0.5}(\Upsilon_+, \Upsilon_-)$ for the analysis cut + MMC for the three different cases. H and Z are stacked. LHC Run 2 data is used (simulated ATLAS $Z \rightarrow \tau\tau$ and $H \rightarrow \tau\tau$ events).

Bibliography

[1] CDF Collaboration,
Observation of Top Quark Production in $\overline{p}p$ Collisions with the Collider Detector at Fermilab,
Phys. Rev. Lett. **74** (14 1995) 2626 (cit. on p. 1).

[2] ATLAS Collarboration, *Observation of a new particle in the search for the Standard Model Higgs boson with the ATLAS detector at the LHC*, Physics Letters B **716** (2012) 1,
ISSN: 0370-2693 (cit. on pp. 1, 13).

[3] CMS Collaboration,
Observation of a new boson at a mass of 125 GeV with the CMS experiment at the LHC,
Physics Letters B **716** (2012) 30, ISSN: 0370-2693 (cit. on pp. 1, 13).

[4] M. Thomson, *Modern particle physics*, Cambridge University Press, 2013 (cit. on pp. 1, 3).

[5] J. F. Gunion, H. E. Haber, G. Kane and D. Sally, *The Higgs hunter's guide*,
Perseus Books, 2000 (cit. on pp. 1, 4, 5).

[6] CMS Collaboration, *Searches for additional Higgs bosons and vector leptoquarks in $\tau\tau$ final states in proton-proton collisions at $\sqrt{s} = 13$ TeV*, CMS-PAS-HIG-21-001, CERN, 2022
(cit. on pp. 1, 2, 5).

[7] *Search for a standard model-like Higgs boson in the mass range between 70 and 110 GeV in the diphoton final state in proton-proton collisions at $\sqrt{s} = 8$ and 13 TeV*,
Physics Letters B **793** (2019) 320, ISSN: 0370-2693 (cit. on pp. 1, 5).

[8] ATLAS Collaboration, *Measurements of Higgs boson production cross-sections in the $H \to \tau^+\tau^-$ decay channel in pp collisions at $\sqrt{s} = 13$ TeV with the ATLAS detector*, 2022,
arXiv: 2201.08269 (cit. on pp. 1, 17, 18, 37).

[9] C. Burgard, *Example: Standard model of physics*,
URL: https://texample.net/tikz/examples/model-physics/ (visited on 05/09/2022)
(cit. on p. 4).

[10] Particle Data Group et al., *Review of Particle Physics*,
Progress of Theoretical and Experimental Physics **2020** (2020) 083C01 (cit. on pp. 4, 6, 7).

[11] P. W. Higgs, *Broken symmetries and the masses of gauge bosons*,
Phys. Rev. Lett. **13** (1964) 508 (cit. on p. 4).

[12] F. Englert and R. Brout, *Broken symmetry and the mass of gauge vector mesons*,
Phys. Rev. Lett. **13** (1964) 321 (cit. on p. 4).

[13] B. Povh, K. Rith, C. Scholz, F. Zetsche and W. Rodejohann, *Teilchen und Kerne: eine Einführung in die physikalischen Konzepte*, Springer-Verlag, 2013 (cit. on pp. 5, 7).

[14] P. Bechtle et al., *The light and heavy Higgs interpretation of the MSSM*, The European Physical Journal C **77** (2017) 67, ISSN: 1434-6044, 1434-6052 (cit. on pp. 5, 6).

[15] F. Domingo, S. Heinemeyer, S. Paßehr and G. Weiglein, *Decays of the neutral Higgs bosons into SM fermions and gauge bosons in the CP-violating NMSSM*, The European Physical Journal C **78** (2018) 942, ISSN: 1434-6044, 1434-6052, arXiv: 1807.06322 (cit. on p. 5).

[16] U. Ellwanger, C. Hugonie and A. M. Teixeira, *The Next-to-Minimal Supersymmetric Standard Model*, Physics Reports **496** (2010) 1, ISSN: 03701573, arXiv: 0910.1785 (cit. on p. 5).

[17] *BSM Higgs production cross sections at* $\sqrt{s} = 13\,\text{TeV}$ *(update in CERN Report4 2016)*, URL: https://twiki.cern.ch/twiki/bin/view/LHCPhysics/CERNYellowReportPageBSMAt13TeV (visited on 15/09/2022) (cit. on p. 5).

[18] M. L. Perl et al., *Evidence for Anomalous Lepton Production in* $e^+ - e^-$ *Annihilation*, Phys. Rev. Lett. **35** (1975) 1489 (cit. on p. 6).

[19] M. C. Hansen, *Studies into measuring the Higgs CP-state in* $H \to \tau\tau$ *decays at ATLAS*, PhD thesis: Universität Bonn, 2020 (cit. on pp. 7, 13).

[20] ATLAS Collaboration, *Reconstruction of hadronic decay products of tau leptons with the ATLAS experiment*, Eur. Phys. J. C **76** (2016) 295, arXiv: 1512.05955 (cit. on pp. 7, 14–16, 20, 28, 30).

[21] B. T. Winter, *Measurement of Tau Polarisation in* $Z/\gamma^* \to \tau\tau$ *Decays in Proton–Proton Collisions at ATLAS*, PhD thesis: Universität Bonn, 2018, 220 pp., URL: https://bonndoc.ulb.uni-bonn.de/xmlui/bitstream/handle/20.500.11811/8063/5546.pdf?sequence=1&isAllowed=y (cit. on pp. 7, 8).

[22] Z. Czyczula, *Measurement of* τ *Polarization in* $W \to \tau\nu$ *Decays with the ATLAS Detector in* pp *Collisions at* $\sqrt{s} = 7\,\text{TeV}$, Nuclear Physics B - Proceedings Supplements **253-255** (2014) 180, ISSN: 09205632, URL: https://linkinghub.elsevier.com/retrieve/pii/S0920563214001753 (visited on 22/08/2022) (cit. on p. 8).

[23] L. K. Schildgen, *Measurement of the* τ *Lepton Polarisation in* $Z \to \tau_{lep}\tau_{had}$ *Decays with the ATLAS Detector*, Master's thesis: Universität Bonn, 2015, URL: https://www.lhc-ilc.physik.uni-bonn.de/ergebnisse/dateien/t00000066.pdf?c=t&id=66 (visited on 24/08/2022) (cit. on p. 8).

[24] I. Deigaard, *Measurement of the Tau Polarization in* $Z \to \tau\tau$ *Decays with the ATLAS Detector*, Master's thesis (cit. on pp. 9, 39).

[25] G. Cowan, "Asimov estimate for discovery significance in counting experiment", Physics Department, Royal Holloway, University of London, 2011 (cit. on p. 10).

[26] *The Large Hadron Collider*, URL: https://home.cern/science/accelerators/large-hadron-collider (visited on 14/09/2022) (cit. on p. 13).

[27] ATLAS Collaboration, *ATLAS data quality operations and performance for 2015-2018 data-taking*, 2020, arXiv: 1911.04632 (cit. on pp. 13, 14, 17).

[28] *The CERN accelerator complex, layout in 2022*, URL: https://cds.cern.ch/record/2800984?ln=en (visited on 14/09/2022) (cit. on p. 14).

[29] ATLAS Collaboration, *The ATLAS Experiment at the CERN Large Hadron Collider*, Journal of Instrumentation **3** (2008) S08003, ISSN: 1748-0221, (visited on 14/09/2022) (cit. on p. 13).

[30] *The ATLAS Detector - Detector & Technology*, URL: https://atlas.cern/Discover/Detector (visited on 14/09/2022) (cit. on p. 13).

[31] *Muon Spectrometer*, URL: https://atlas.cern/Discover/Detector/Muon-Spectrometer (visited on 14/09/2022) (cit. on p. 13).

[32] *Computer generated image of the whole ATLAS detector*, URL: https://cds.cern.ch/record/1095924 (visited on 14/09/2022) (cit. on p. 15).

[33] *Experimental particle physics - units, quanitities, kinematics, measurements*, URL: https://indico.cern.ch/event/294651/contributions/671927/attachments/552039/760667/Delmastro_ESIPAP2014_1.pdf (visited on 15/09/2022) (cit. on p. 13).

[34] *The Inner Detector*, URL: https://atlas.cern/Discover/Detector/Inner-Detector (visited on 10/10/2022) (cit. on p. 14).

[35] *Calorimeter*, URL: https://atlas.cern/Discover/Detector/Calorimeter (visited on 10/10/2022) (cit. on p. 15).

[36] M. Cacciari, G. P. Salam and G. Soyez, *The anti-k_t jet clustering algorithm*, Journal of High Energy Physics **2008** (2008) 063 (cit. on p. 15).

[37] *SM Higgs production cross sections at $\sqrt{s}$ = 13, 14 and 27 TeV*, URL: https://twiki.cern.ch/twiki/bin/view/LHCPhysics/CERNHLHE2019 (visited on 15/10/2022) (cit. on p. 17).

[38] *Trigger and Data Acquisition*, URL: https://atlas.cern/Discover/Detector/Trigger-DAQ (visited on 07/10/2022) (cit. on p. 18).

[39] ATLAS Collaboration, *Identification of hadronic tau lepton decays using neural networks in the ATLAS experiment*, tech. rep., All figures including auxiliary figures are available at https://atlas.web.cern.ch/Atlas/GROUPS/PHYSICS/PUBNOTES/ATL-PHYS-PUB-2019-033: CERN, 2019, URL: http://cds.cern.ch/record/2688062 (cit. on p. 20).

[40] A. Elagin, P. Murat, A. Pranko and A. Safonov,
A New Mass Reconstruction Technique for Resonances Decaying to di-tau,
Nuclear Instruments and Methods in Physics Research Section A: Accelerators, Spectrometers, Detectors and Associated Equipment **654** (2011) 481, ISSN: 01689002 (cit. on p. 20).

List of Figures

List of Tables